The Astrophysical Journal, 754:21 (16pp), 2012 July 20 doi:10.1088/0004-637X/754/1/21

ROSSBY WAVE INSTABILITY IN LOCALLY ISOTHERMAL AND POLYTROPIC DISKS: THREE-DIMENSIONAL LINEAR CALCULATIONS

Min-Kai Lin
Canadian Institute for Theoretical Astrophysics, 60 St. George Street, Toronto, ON M5S 3H8, Canada; mklin924@cita.utoronto.ca
Received 2012 March 5; accepted 2012 May 14; published 2012 June 29

ABSTRACT

Numerical calculations of the linear Rossby wave instability (RWI) in global three-dimensional (3D) disks are presented. The linearized fluid equations are solved for vertically stratified, radially structured disks with either a locally isothermal or polytropic equation of state, by decomposing the vertical dependence of the perturbed hydrodynamic quantities into Hermite and Gegenbauer polynomials, respectively. It is confirmed that the RWI operates in 3D. For perturbations with vertical dependence assumed above, there is little difference in growth rates between 3D and two-dimensional (2D) calculations. Comparison between 2D and 3D solutions of this type suggests the RWI is predominantly a 2D instability and that 3D effects, such as vertical motion, can be interpreted as a perturbative consequence of the dominant 2D flow. The vertical flow around corotation, where vortex formation is expected, is examined. In locally isothermal disks, the expected vortex center remains in approximate vertical hydrostatic equilibrium. For polytropic disks, the vortex center has positive vertical velocity, whose magnitude increases with decreasing polytropic index n.

Key words: accretion, accretion disks – hydrodynamics – instabilities – methods: numerical

Online-only material: color figures

1. INTRODUCTION

Theoretical modeling of protoplanetary disks leads to complex structures that are unlikely to be described by smooth radial profiles (Terquem 2008; Armitage 2011). However, radially structured disks may develop the Rossby wave instability (RWI; Lovelace et al. 1999; Li et al. 2000), which leads to vortex formation in the nonlinear regime (Li et al. 2001). Thus, the RWI may play a role in the evolution of protoplanetary disks.

The disk RWI is a dynamical instability associated with the presence of extrema in the ratio of vorticity to surface density, or vortensity.[1] The instability results from wave coupling across such an extremum. Its physics is similar to the Papaloizou–Pringle instability (PPI; Papaloizou & Pringle 1984, 1985, 1987; Goldreich et al. 1986; Narayan et al. 1987) which operates in pressure-supported, thick tori. The RWI operates in thin, centrifugally supported disks with non-power-law rotation profiles, and is insensitive to radial boundary conditions.

The relevance of the RWI in protoplanetary disks has been demonstrated in two situations. Variability in the efficiency of turbulent angular momentum transport by the magneto-rotational instability (Balbus & Hawley 1991) can result in the existence of "dead zones" (Gammie 1996), in which the turbulent viscosity is small. The radial boundary between a dead zone and the actively accreting region is prone to the RWI (Varnière & Tagger 2006; Lyra et al. 2008, 2009; Crespe et al. 2011), with observable consequences (Regály et al. 2012). In addition to hydrodynamic angular momentum transport, the RWI may also assist planet formation by concentrating solids into anti-cyclonic vortices (Barge & Sommeria 1995).

Another origin of the RWI in protoplanetary disks, which motivated this study, is disk–planet interaction (Goldreich & Tremaine 1979, 1980). A sufficiently massive planet leads to gap opening (Lin & Papaloizou 1986), while low-mass protoplanets may open gaps provided the disk viscosity is sufficiently small (Muto et al. 2010; Dong et al. 2011). Vortensity jumps across planet-induced shocks lead to the necessary disk profile for the RWI to develop around gap edges (Koller et al. 2003; Li et al. 2005; de Val-Borro et al. 2007). Subsequent vortex formation significantly affects disk–planet torques and migration (Ou et al. 2007; Li et al. 2009; Yu et al. 2010; Lin & Papaloizou 2010).

The above studies of the RWI have all employed the razor-thin-disk approximation (but note that the PPI was originally analyzed in three dimensions (3D)). Yu & Li (2009) have examined the RWI with a toroidal magnetic field in a 3D but unstratified disk. Meheut et al. (2010) first demonstrated the RWI in nonlinear hydrodynamic simulations of 3D stratified disks (later with improved resolution in Meheut et al. 2012a), while Umurhan (2010) analyzed the RWI in approximate 3D disk models.

Recently, Meheut et al. (2012b) calculated linear RWI modes in a three-dimensional, globally isothermal disk, which displayed vertical motion. In this paper, we compute linear RWI modes in 3D disks across a range of parameter values, including different equations of state. Our focus here is on how these affect the vertical flow in the corotation region, where vortex formation is known to occur (Li et al. 2001).

This paper is organized as follows. In Section 2, we list the governing equations and describe our disk models. We derive the linearized fluid equations in Section 3 and describe our numerical methods in Section 4. Results are presented in Section 5 for locally isothermal disks and in Section 6 for polytropic disks. In Section 7, we briefly examine a linear mode qualitatively different from those above, found in a disk model involving $\kappa^2 < 0$ (taken from Meheut et al. 2010), where κ is the epicycle frequency. We summarize and discuss our results in Section 8, including limitations of our calculations.

2. GOVERNING EQUATIONS, DISK MODELS AND ASSUMPTIONS

We consider a three-dimensional, inviscid, non-self-gravitating disk orbiting a star of mass M_* and adopt (r, ϕ, z)

[1] This quantity is modified by a factor involving the disk entropy, if the latter is not constant.

cylindrical polar coordinates centered on the star. The frame is non-rotating. The governing equations are the 3D Euler equations:

$$\frac{\partial \rho}{\partial t} + \nabla \cdot (\rho \boldsymbol{v}) = 0, \tag{1}$$

$$\frac{\partial \boldsymbol{v}}{\partial t} + \boldsymbol{v} \cdot \nabla \boldsymbol{v} = -\frac{1}{\rho} \nabla P - \nabla \Phi_*, \tag{2}$$

$$P = P(r, \rho), \tag{3}$$

where ρ is the density, P is the pressure, $\boldsymbol{v}$ is the velocity field, and Φ_* is the gravitational potential due to the central star. Equation (3) is an equation of state (EOS), specified later, such that the pressure may be calculated without an energy equation.

We assume the disk is geometrically thin so that Φ_* may be approximated as

$$\Phi_*(r, z) = -\frac{GM_*}{\sqrt{r^2 + z^2}} \simeq -\frac{GM_*}{r}\left(1 - \frac{z^2}{2r^2}\right). \tag{4}$$

This approximation is adopted so that the resulting equilibrium density field has a convenient functional form suitable for the application of orthogonal polynomials (see Section 4). This greatly simplifies the numerical problem. Henceforth, we use the approximate potential for self-consistency.

The unperturbed disk is steady, axisymmetric with no meridional velocity ($\partial_t = \partial_\phi = v_r = v_z = 0$). The disk is stratified with $\rho = \rho(r, z)$ set by vertical hydrostatic balance. The azimuthal velocity is $v_\phi = r\Omega$, where Ω is the angular speed. v_ϕ is set by radial balance between pressure, stellar gravity, and centrifugal forces. Because the disk is thin, the angular velocity is close to Keplerian, i.e., $\Omega \simeq \Omega_k \equiv (GM_*/r^3)^{1/2}$.

To introduce radial structure, we choose the unperturbed surface density profile to be

$$\Sigma(r) \equiv \int_{-\infty}^{\infty} \rho dz = \Sigma_0 \left(\frac{r}{r_0}\right)^{-\alpha} \times \left\{1 + (\mathcal{A} - 1) \exp\left[-\frac{(r - r_0)^2}{2\Delta r^2}\right]\right\} \tag{5}$$

(Li et al. 2000). Equation (5) corresponds to a Gaussian surface density bump centered at $r = r_0$, width Δr, and amplitude $\mathcal{A}$, on top of a background power-law profile with index $-\alpha$. Since disk self-gravity is ignored, the surface density scale Σ_0 is arbitrary.

To specify the 3D disk structure, we choose the EOS to be either locally isothermal or polytropic. These are described below.

2.1. Locally Isothermal Disks

For locally isothermal disks, the pressure is calculated as

$$P = c_s^2(r)\rho, \tag{6}$$

where $c_s(r)$ is the sound speed given by $c_s = H\Omega_k$ and $H(r)$ is the disk scale height. The unperturbed density is

$$\rho(r, z) = \frac{\Sigma(r)}{\sqrt{2\pi}H(r)} \exp\left[-\frac{z^2}{2H^2(r)}\right]. \tag{7}$$

In the numerical calculations, we will choose $H(r) = hr$ with h being a constant aspect ratio, since this is a typical model for protoplanetary disks.[2] The exponential decay means the gas density becomes negligible after a few scale heights. Thus, the vertical domain can be taken to be $z \in [-\infty, \infty]$, even though we have made the thin-disk approximation.

2.1.1. Approximate Equilibrium

For simplicity, we set the azimuthal velocity to

$$v_\phi^2 = \frac{r}{\rho}\frac{\partial P}{\partial r}\bigg|_{z=0} + r\frac{\partial \Phi_*}{\partial r}\bigg|_{z=0}. \tag{8}$$

Away from the midplane, the deviation from exact radial balance is proportional to $h^2 \ll 1$ for a thin disk (Tanaka et al. 2002). We adopt Equation (8) to allow us to apply standard solution methods.

To test whether or not the precise form of Ω affects our results, we also considered setting $\rho \to \Sigma$ in Equation (8), which gives the velocity profile $v_{\phi,2D}$ for a razor-thin disk. For our fiducial calculation, growth rates differ by $\sim$1% between adopting Equation (8) or $v_{\phi,2D}$, and we observe the same flow structure.

In fact, locally isothermal disks generally have differential rotation in z, i.e., $\Omega = \Omega(r, z)$, unless the disk is also globally isothermal. It is therefore important to note that in assuming Equation (8), we have artificially suppressed baroclinic effects. We discuss some justification for this in Section 8.4 and Appendix A. Although the chosen basic state is not in exact equilibrium, setting $\Omega = \Omega(r)$ greatly simplifies the linear equations as the only vertical dependence of the basic state is through the exponential factor in ρ. It allows us to address the specific question of whether or not vertical density stratification has any effect on the RWI, without the complication of baroclinic instabilities (Knobloch & Spruit 1986; Umurhan 2012).

2.2. Polytropic Disks

In order to set up a more self-consistent basic state, that is, $\Omega = \Omega(r)$ and a finite vertical domain, we also consider polytropic disks, for which

$$P = K\rho^{1+\frac{1}{n}}, \tag{9}$$

where K is a constant and n is the polytropic index. Vertical hydrostatic equilibrium implies

$$\rho(r, z) = \left[\frac{GM_*H^2(r)}{2K(1+n)r^3}\right]^n \left[1 - \frac{z^2}{H^2(r)}\right]^n \equiv \rho_0(r)\left[1 - \frac{z^2}{H^2(r)}\right]^n. \tag{10}$$

Here, $z = H$ is the disk surface where $\rho(r, H) = 0$. Thus, when discussing polytropic disks H is referred to as the disk thickness.

The function $H(r)$ and midplane density $\rho_0(r)$ are calculated through

$$\Sigma(r) = \rho_0(r)H(r)I_n, \tag{11}$$

where $I_n \equiv \int_{-1}^{1}(1 - x^2)^n dx$, with $\rho_0(r)$ related to $H(r)$ by Equation (10) and $\Sigma(r)$ given by Equation (5). We can therefore write

$$H(r) = H_0\left[\frac{\Sigma(r)}{\mathcal{A}\Sigma_0}\right]^{\frac{1}{2n+1}}\left(\frac{r}{r_0}\right)^{\frac{3n}{2n+1}}, \tag{12}$$

[2] This choice also enables us to compare the locally isothermal disk with a polytropic disk with constant aspect ratio.

where $H_0 = H(r_0)$ is the disk thickness *at the bump radius*. We parameterize it by writing $H_0 = hr_0$ so that h is the aspect ratio at r_0. Note that a surface density enhancement by a factor $\mathcal{A}$ corresponds to an enhancement of the disk thickness by a factor $\mathcal{A}^{1/(2n+1)}$.

For a polytropic disk, the azimuthal velocity is strictly independent of z (e.g., Papaloizou & Pringle 1984). It is given by

$$v_\phi^2(r) = r\frac{\partial}{\partial r}\Phi_*(r, H) = \frac{GM_*}{r}\left(1 - \frac{3H^2}{2r^2} + \frac{H}{r}\frac{dH}{dr}\right), \quad (13)$$

where the second equality follows from the approximation for the stellar potential in a thin disk (Equation (4)).

Of course, given $H(r)$ one can obtain the azimuthal velocity $v_{\phi,e}$ corresponding to the exact gravitational potential of a point mass. For our fiducial setup, the difference in growth rate is <4% between using $v_{\phi,e}$ and using v_ϕ above, and we observe no difference in flow structure. However, we will use v_ϕ so that the equilibrium density and velocity fields are self-consistent and in exact balance with the same potential.

3. LINEARIZED EQUATIONS

In this section, we derive the governing equation for small disturbances in the disk. As described above, the basic state is $\rho = \rho(r, z)$ and $\boldsymbol{v} = (0, r\Omega, 0)$, with $\Omega = \Omega(r)$. The perturbed state is assumed to have the form

$$\rho \rightarrow \rho + \mathrm{Re}[\delta\rho(r, z)\exp i(\sigma t + m\phi)], \quad (14)$$

$$P \rightarrow P + \mathrm{Re}[\delta P(r, z)\exp i(\sigma t + m\phi)], \quad (15)$$

$$\boldsymbol{v} \rightarrow \boldsymbol{v} + \mathrm{Re}[\delta\boldsymbol{v}(r, z)\exp i(\sigma t + m\phi)], \quad (16)$$

where $\sigma = \sigma_R + i\gamma$ is a complex frequency (σ_R, γ being real) and m is the azimuthal wavenumber taken to be a positive integer. We will omit writing "Re" below, with the understanding that physical solutions correspond to real parts of the complex perturbations.

For the locally isothermal EOS, the linearized momentum equations give

$$\delta v_r = -\frac{ic_s^2}{D}\left(\bar{\sigma}\frac{\partial W}{\partial r} + \frac{2m\Omega W}{r}\right), \quad (17)$$

$$\delta v_\phi = \frac{c_s^2}{D}\left(\frac{\kappa^2}{2\Omega}\frac{\partial W}{\partial r} + \frac{\bar{\sigma}mW}{r}\right), \quad (18)$$

$$\delta v_z = \frac{ic_s^2}{\bar{\sigma}}\frac{\partial W}{\partial z}, \quad (19)$$

where $W \equiv \delta\rho/\rho$ is the relative density perturbation, $\bar{\sigma} \equiv \sigma + m\Omega(r)$ is the shifted frequency, $D \equiv \kappa^2 - \bar{\sigma}^2$, and

$$\kappa^2 = \frac{1}{r^3}\frac{\partial}{\partial r}(r^4\Omega^2) \quad (20)$$

is the square of the epicycle frequency. Corresponding equations for the polytropic disk are very similar, and are readily obtained by setting c_s to unity and replacing $W \rightarrow S \equiv \delta P/\rho$, where S is the enthalpy perturbation.

Inserting the perturbed velocity field into the linearized continuity equation,

$$i\bar{\sigma}\delta\rho + \frac{1}{r}\frac{\partial}{\partial r}(r\rho\delta v_r) + \frac{im}{r}\rho\delta v_\phi + \frac{\partial}{\partial z}(\rho\delta v_z) = 0, \quad (21)$$

yields, for locally isothermal disks:

$$r\delta\rho = \frac{\partial}{\partial r}\left(\frac{r\rho c_s^2}{D}\frac{\partial W}{\partial r}\right) + \frac{2mW}{\bar{\sigma}}\frac{\partial}{\partial r}\left(\frac{c_s^2\rho\Omega}{D}\right) - \left(\frac{m^2c_s^2\rho}{rD}\right)W - \frac{rc_s^2}{\bar{\sigma}^2}\frac{\partial}{\partial z}\left(\rho\frac{\partial W}{\partial z}\right), \quad (22)$$

and for polytropic disks:

$$r\delta\rho = \frac{\partial}{\partial r}\left(\frac{r\rho}{D}\frac{\partial S}{\partial r}\right) + \frac{2mS}{\bar{\sigma}}\frac{\partial}{\partial r}\left(\frac{\rho\Omega}{D}\right) - \left(\frac{m^2\rho}{rD}\right)S - \frac{r}{\bar{\sigma}^2}\frac{\partial}{\partial z}\left(\rho\frac{\partial S}{\partial z}\right). \quad (23)$$

We remark that Equation (22) is in fact valid for locally isothermal disks with any fixed sound-speed profile $c_s(r)$, assuming the equilibrium azimuthal velocity is independent of z (Appendix A). Also note that Equation (23) is actually valid for any barotropic EOS , i.e., whenever $P = P(\rho)$. The 3D problem is to solve Equations (22) and (23), which will generally describe disturbances depending on (r, ϕ, z) and motion in all three directions.

3.1. Relation to the Two-dimensional Problem

We define the two-dimensional (2D) problem as solving Equations (22) and (23) subject to $\partial_z = 0$. Denoting the corresponding solutions as $W_{2D}(r)$, $S_{2D}(r)$ and inserting them into the governing equations yields, after vertical integration,

$$r\delta\Sigma = \frac{d}{dr}\left(\frac{r\Sigma c_s^2}{D}\frac{dW_{2D}}{dr}\right) + \frac{2mW_{2D}}{\bar{\sigma}}\frac{d}{dr}\left(\frac{c_s^2\Sigma\Omega}{D}\right) - \left(\frac{m^2c_s^2}{rD}\right)\Sigma W_{2D} \quad (24)$$

for locally isothermal disks and

$$r\delta\Sigma = \frac{d}{dr}\left(\frac{r\Sigma}{D}\frac{dS_{2D}}{dr}\right) + \frac{2mS_{2D}}{\bar{\sigma}}\frac{d}{dr}\left(\frac{\Sigma\Omega}{D}\right) - \left(\frac{m^2\Sigma}{rD}\right)S_{2D} \quad (25)$$

for polytropic disks, where $\delta\Sigma = \int_{-\infty}^{\infty}\delta\rho dz$ is the surface density perturbation. Note that $W_{2D} = \delta\Sigma/\Sigma$ is the relative surface density perturbation, and $S_{2D} = \delta\Pi/\Sigma$ where $\delta\Pi$ is the perturbation to the vertically integrated pressure ($\Pi = \int_{-\infty}^{\infty}Pdz$). Solutions to Equations (24) and (25) describe disturbances which only depend on (r, ϕ) and there is no vertical motion.

As defined here, the 2D problem and the 3D problem involve the same background disk, which is three dimensional. However, the governing equation for linear disturbances in razor-thin disks have the same form as Equations (24) and (25) when the razor-thin disk has a locally isothermal or barotropic EOS in the form $\Pi = c_s^2(r)\Sigma$ or $\Pi = \Pi(\Sigma)$, respectively.

3.2. Corotation Singularity and the RWI

Inspection of the 2D equations, Equations (24) and (25), reveals a potential singularity when $\bar{\sigma}(r_c) = 0$, where r_c is the corotation radius defined by

$$\sigma_R + m\Omega(r_c) = 0. \tag{26}$$

This corotation singularity can be rendered ineffective if r_c also satisfies

$$\frac{d}{dr}\left(\frac{c_s^2}{\eta}\right)\bigg|_{r_c} = 0 \quad \text{for locally isothermal disks,} \tag{27}$$

$$\frac{d}{dr}\left(\frac{1}{\eta}\right)\bigg|_{r_c} = 0 \quad \text{for polytropic disks,} \tag{28}$$

where

$$\eta \equiv \frac{\kappa^2}{2\Omega\Sigma} \tag{29}$$

is the vortensity. The quantity η/c_s^2 can be seen as a generalized vortensity (Li et al. 2000), but for convenience we will simply use "vortensity" in the discussion below. Thus, there can exist 2D neutral disturbances with corotation at a vortensity extremum, for which the 2D linear operator is real and regular everywhere.

Strictly speaking, corotation singularities only concern neutral disturbances ($\gamma = 0$). In practice, we are interested in growing solutions ($\gamma < 0$) so such singularities do not arise in the numerical computation. Nevertheless, the discussion above is important because the growth rates we find are typically $|\gamma| \ll \Omega(r_0)$. Furthermore, association of r_c with a vortensity extremum forms the basis of the RWI.

In studies employing razor-thin disks, the RWI has the largest disturbance amplitude in the corotation region where $|\bar{\sigma}^2| \ll \kappa^2$. It can be shown that such modes can only be unstable if vortensity extrema exist in the disk (e.g., Lin & Papaloizou 2010). Indeed, the RWI is found to have with corotation radius r_c close to a vortensity minimum (Lovelace et al. 1999; Li et al. 2000; Lin & Papaloizou 2011a).

It is precisely linear modes with the above properties which we wish to explore in 3D. However, we do not expect such modes to have significant z-dependence in their relative density or enthalpy perturbation around corotation. From the linearized vertical equation of motion, we see that

$$\delta v_z \propto \frac{1}{\bar{\sigma}}\frac{\partial X}{\partial z},$$

where X is W or S depending on the EOS. Near corotation where $|\bar{\sigma}|$ is small, $|\partial_z X|$ should be almost negligible. Otherwise, even small vertical gradients in density or enthalpy perturbation will cause significant vertical motion, and linearization becomes invalid.

4. NUMERICAL PROCEDURE

In principle, one could attempt a numerical solution to the partial differential equations (PDEs) above, for example, by finite differencing in the (r, z) plane. However, since one of our goals is to assess 3D effects, it is more useful to have a numerical scheme that automatically separates out the 2D problem from the full 3D problem.

We begin by making the coordinate transformation

$$(\hat{r}, \hat{z}) \equiv (r, z/H), \tag{30}$$

$$\left(\frac{\partial}{\partial r}, \frac{\partial}{\partial z}\right) = \left(\frac{\partial}{\partial \hat{r}} - \hat{z}\frac{H'}{H}\frac{\partial}{\partial \hat{z}}, \frac{1}{H}\frac{\partial}{\partial \hat{z}}\right), \tag{31}$$

where the prime denotes differentiation with respect to the argument. In this coordinate system, the background density is separable, i.e., $\rho(\hat{r}, \hat{z}) = g(\hat{r})f(\hat{z})$, where $f = \exp(-\hat{z}^2/2)$ for locally isothermal disks and $f = (1 - \hat{z}^2)^n$ for polytropic disks. This motivates us to seek solutions of the form

$$W = \sum_{l=0}^{\infty} W_l(\hat{r})\mathcal{H}_l(\hat{z}), \tag{32}$$

$$S = \sum_{l=0}^{\infty} S_l(\hat{r})\mathcal{C}_l^{\lambda}(\hat{z}), \tag{33}$$

where $\mathcal{H}_l$ is a Hermite polynomial of order l and $\mathcal{C}_l^{\lambda}$ is a Gegenbauer polynomial of index λ and order l. Note that radial and vertical variations are coupled because $\hat{z} = \hat{z}(r)$ through $H(r)$.

These polynomials satisfy the orthogonality relations

$$\int_{-\infty}^{\infty} \mathcal{H}_k(\hat{z})\mathcal{H}_l(\hat{z})\exp(-\hat{z}^2/2)d\hat{z} = \sqrt{2\pi}l!\delta_{kl}, \tag{34}$$

$$\int_{-1}^{1} \mathcal{C}_k^{\lambda}(\hat{z})\mathcal{C}_l^{\lambda}(\hat{z})(1-\hat{z}^2)^{\lambda-1/2}d\hat{z} = \frac{\pi 2^{1-2\lambda}\Gamma(l+2\lambda)}{l!(l+\lambda)\Gamma^2(\lambda)}\delta_{kl}, \tag{35}$$

where δ_{kl} here is the Kronecker delta and Γ is the Gamma function (Abramowitz & Stegun 1965). For polytropic disks, we choose the parameter λ to be

$$\lambda = n - \frac{1}{2}. \tag{36}$$

Consequently, for a polytropic index $n = 1.5$, $\mathcal{C}_l^1$ are the Chebyshev polynomials of the second kind, and for $n = 1$, $\mathcal{C}_l^{1/2}$ are the Legendre polynomials. Eigenfunction expansions in $\hat{z}$ is a standard method to account for vertical dependence in disk problems (e.g., Okazaki & Kato 1985; Papaloizou & Pringle 1985; Takeuchi & Miyama 1998; Tanaka et al. 2002).

It is important to keep in mind that by assuming the above decompositions (Equations (32) and (33)) we restrict the type of perturbations to those satisfying certain physical conditions implied by the orthogonal polynomials at the upper disk boundary. In the locally isothermal disk, we require the kinetic energy density to be bounded at large heights (Takeuchi & Miyama 1998), and for polytropic disks a regularity condition applies at $\hat{z} = \pm 1$ (Papaloizou & Pringle 1985). Such perturbations can be decomposed as above because the polynomials form a complete set (Zhang & Lai 2006). On the other hand, the above specific decomposition cannot be applied if one considers other vertical boundary conditions (e.g., conditions imposed at other heights).

After transforming the governing equations into $(\hat{r}, \hat{z})$ coordinates, we insert the ansatz equations (32) and (33) into Equations (22) and (23), multiply by $\mathcal{H}_k$, and $\mathcal{C}_k^{\lambda}$, respectively, then integrate vertically. This procedure yields an equation of the form

$$A_l X_l + B_l X_{l-2} + C_l X_{l+2} = 0, \tag{37}$$

where X_l is W_l or S_l, and A_l, B_l, and C_l are linear operators which only depend on r and σ, but are different for the two EOSs (see Appendix A). For each l, there is a separate equation with the operators B_l, C_l representing coupling with the $l \pm 2$ modes. Note that B_l is set to zero when $l = 0,\ 1$.

We have now transformed the governing PDE into an infinite set of coupled ordinary differential equations (ODEs). In practice, we truncate the solution at $l_{\max}$, i.e., $X_l \equiv 0$ for $l > l_{\max}$. The decomposition has the advantage that for modes nearly independent of z, $l_{\max}$ can be small. In the simplest case of setting $l_{\max} = 0$, we only solve

$$A_0 X_0 = 0, \tag{38}$$

which is the 2D problem. That is, if $l_{\max} = 0$ then $W_0 = W_{2D}$ and $S_0 = S_{2D}$.

4.1. Matrix Methods

We now proceed to a numerical solution to the linear problem. We discretize the linear operators and solutions on a grid which divides the radial range $r \in [r_i, r_o]$ into N_r uniformly spaced points. The coupled set of ODEs then becomes a single matrix equation. This is denoted generically as

$$\boldsymbol{M}\boldsymbol{x} = \boldsymbol{0}, \tag{39}$$

where the square matrix $\boldsymbol{M}$ represents the discretized linear operator and the vector $\boldsymbol{x}$ is the discretized solution. The size of the matrix and vector depends on $l_{\max}$. For example, setting $l_{\max} = 4$, Equation (39) then represents the discretized version of

$$\begin{aligned} A_0 X_0 + C_0 X_2 &= 0, \\ B_2 X_0 + A_2 X_2 + C_2 X_4 &= 0, \\ B_4 X_2 + A_4 X_4 &= 0, \end{aligned}$$

for which $\boldsymbol{M}$ is a $3N_r \times 3N_r$ matrix and $\boldsymbol{x}$ is a vector of length $3N_r$.

The matrix problem, Equation (39), is a set of homogeneous linear equations. Non-trivial solutions exist if

$$\det \boldsymbol{M} = 0. \tag{40}$$

The complex frequency σ is required to be such that the matrix $\boldsymbol{M}(\sigma)$ is singular. We have used two approaches to achieve this. The first is to consider the usual eigenvalue problem:

$$\boldsymbol{M}(\sigma)\boldsymbol{x} = \nu \boldsymbol{x}. \tag{41}$$

Starting with a trial σ, standard matrix software[3] may be used to find the eigenvalues ν and associated eigenvectors $\boldsymbol{x}$. We then apply Newton–Raphson iteration to solve $\nu_{\min}/|\nu_{\max}| = 0$ by varying σ, where $\nu_{\min,\max}$ corresponds to eigenvalues of smallest and largest absolute value found from Equation (41).

Another approach is to perform a singular value decomposition[4] (SVD) of $\boldsymbol{M}$, so that

$$\boldsymbol{M} = \boldsymbol{U}\,\mathrm{diag}(s_1, s_2, \ldots)\boldsymbol{V}^\dagger, \tag{42}$$

where $\boldsymbol{U}$ and $\boldsymbol{V}$ are unitary matrices ("$\dagger$" denotes Hermitian conjugate) and the real numbers $s_i \geqslant 0$ are the singular values of $\boldsymbol{M}$. The columns of $\boldsymbol{V}$ are the right singular vectors of $\boldsymbol{M}$. If $\min(s_i) = 0$ then $\boldsymbol{M}\boldsymbol{x}_0 = \boldsymbol{0}$, where $\boldsymbol{x}_0$ is the right singular vector associated with $\min(s_i)$. We therefore use Newton–Raphson iteration to zero the quantity $F \equiv \boldsymbol{x}_0^\dagger \boldsymbol{M}\boldsymbol{x}_0 / \boldsymbol{x}_0^\dagger \boldsymbol{x}_0$ by varying σ.

These methods give the same result. We always perform the SVD for the final matrix $\boldsymbol{M}(\sigma)$ in order to evaluate R^{-1}, where $R \equiv \max(s_i)/\min(s_i)$ is the condition number of $\boldsymbol{M}$. Since $R = \infty$ for a singular matrix, we only accept solutions for which R^{-1} is zero at machine precision (typically $R^{-1} \lesssim 10^{-15}$). The matrix methods outlined above were also used in Lin & Papaloizou (2011a, 2011b).

4.2. Radial Boundary Conditions

For simplicity, we impose $dX_l/dr = 0$ at $r = r_i, r_o$. The RWI is associated with internal structure away from boundaries. Consequently, it is insensitive to radial boundary conditions in razor-thin disks (de Val-Borro et al. 2007; Lin & Papaloizou 2011a). We assume this still holds in 3D. For example, approximate 3D disk models developed by Umurhan (2008, 2010), in which the inner/outer disk boundaries play no role, also support the RWI.

As a check, additional calculations were performed with $\partial_r X = 0$ applied at boundaries (which introduces mode coupling), different r_i, r_o, and a numerical condition where boundary derivatives are approximated by interior points. The last case is strictly a numerical procedure to generate a closed set of equations to solve. For the solutions of interest, these experiments gave results with no appreciable difference.

4.3. Fiducial Setup

We work in units such that $G = M_* = 1$. Our standard disk spans $r \in [r_i, r_o] = [0.4, 1.6]$ and has a surface density profile with $\alpha = 0.5$. The bump is located at $r_0 = 1$ with width parameter $\beta = 0.05$. We use $N_r = 512$ grid points and first solve the 2D problem ($l_{\max} = 0$), then use the obtained eigenvalue to start the iteration for the 3D problem, for which $l_{\max} = 6$. We only consider even l.

In Section 7, we will use the setup employed by Meheut et al. (2010) to examine a 3D RWI mode with $\kappa^2 < 0$ at the bump radius. This mode appears quite different from our standard setup with $\kappa^2 > 0$ everywhere.

4.4. Results Analysis

The solution to the linear problem gives the complex radial functions X_l, which can be used to reconstruct the complex amplitudes, e.g., $\delta v_z(r, z)$ by using Equations (32), (33), and (19), but we are interested in physical (real) solutions. We will often visualize the solution for a specific m with 2D plots. We explain below how these are obtained.

The real perturbation is, e.g., $\mathrm{Re}[\delta v_z \exp i(\sigma t + m\phi)$, so the spatial dependence of a physical perturbation is

$$\delta v_z \to \mathrm{Re}[\delta v_z]\cos(m\phi) - \mathrm{Im}[\delta v_z]\sin(m\phi), \tag{43}$$

and similarly for other variables. We focus on the solution near the *vortex core*, defined to be at $(r, \phi) = (r_0, \phi_0)$, where

$$\begin{aligned} \cos(m\phi_0) &= \mathrm{Re}[X(r_0, 0)]/|X(r_0, 0)|, \\ \sin(m\phi_0) &= -\mathrm{Im}[X(r_0, 0)]/|X(r_0, 0)|. \end{aligned} \tag{44}$$

[3] We used LAPACK.

[4] We used LAPACK for a direct decomposition. We also performed the SVD with PROPACK (available at http://soi.stanford.edu/~rmunk/PROPACK/), which is an iterative method. These gave the same results.

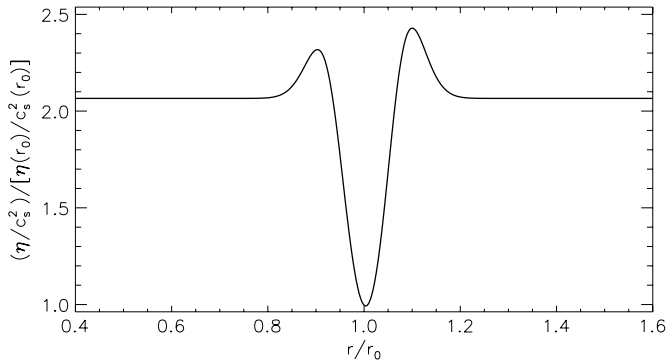

Figure 1. Background profile of the fiducial locally isothermal disk with $\mathcal{A} = 1.25$ and $h = 0.07$, in terms of the generalized vortensity η/c_s^2, scaled by its value at the bump. Unstable modes are associated with the minimum at r_0.

Table 1
Eigenfrequencies in the Locally Isothermal Disk with $h = 0.07$

m	$-\sigma_R/(m\Omega_0)$	$-10^2\gamma/\Omega_0$
1	0.9960 (0.9960)	2.8038 (2.8044)
2	0.9960 (0.9960)	4.8931 (4.8985)
3	0.9961 (0.9960)	5.7205 (5.7365)
4	0.9964 (0.9964)	5.1245 (5.1843)
5	0.9972 (0.9971)	3.4557 (3.5720)
6	0.9980 (0.9978)	1.8317 (1.9615)

Note. Values in brackets were obtained from the 2D problem.

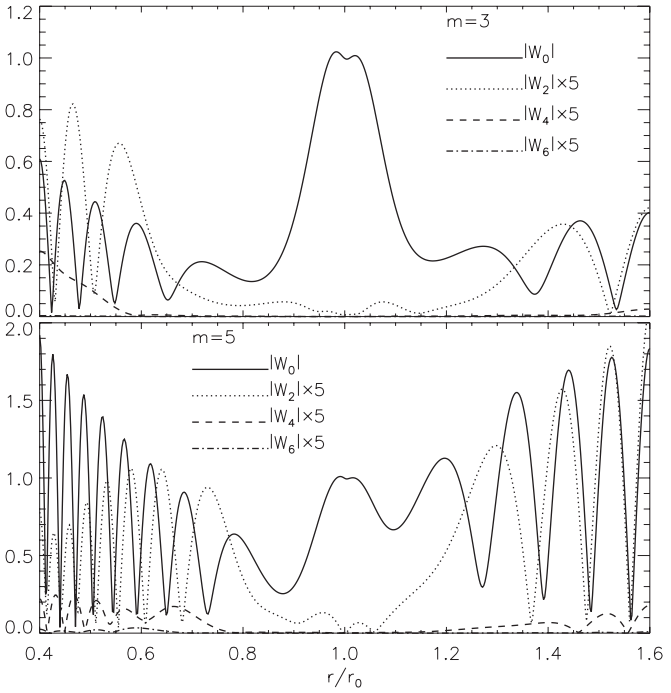

Figure 2. Radial eigenfunctions W_l for locally isothermal disk with $h = 0.07$. These are normalized by $|W_0(r_0)|$. The $l > 0$ modes have also been magnified in order to compare its radial structure with W_0.

The magnitude of the (real) perturbation is arbitrary but its sign is fixed, e.g., X, now representing the real density or enthalpy perturbation, is positive at $(r, \phi, z) = (r_0, \phi_0, 0)$. In practice, the vortex core is near a maximum midplane overdensity.

We visualize results in the (r, z) plane by setting $\phi = \phi_0$ in Equation (43). Similarly, perturbations are visualized in the (r, ϕ) plane at a chosen z, and in the (ϕ, z) plane at $r = r_0$ with the azimuthal range set to $\phi \in [\phi_0 - \pi/2m, \phi_0 + \pi/2m]$. For convenience, we also define $\Omega_0 \equiv \Omega(r_0)$ and $\kappa_0 \equiv \kappa(r_0)$.

5. RESULTS: LOCALLY ISOTHERMAL DISKS

For locally isothermal disks, we choose $h = 0.07$ and $\mathcal{A} = 1.25$ as a fiducial case. Recall $c_s^2 \propto 1/r$, so that far from r_0 the generalized vortensity η/c_s^2 is flat, and is a minimum at r_0. The background disk is shown in Figure 1. Note that $\kappa^2 > 0$ everywhere, and $\min(\kappa^2/\Omega_k^2) \simeq 0.59$.

Recall that for locally isothermal disks, we assumed an approximate basic state (Section 2.1.1). The extent of inexact radial balance in the background depends on h (Tanaka et al. 2002). In a nonlinear simulation, this may lead to radial motion. To keep this effect fixed in comparing different linear calculations below, in this section we fix h.

5.1. Solution Example

We solved the fiducial case for $m \in [1, 6]$. Table 1 compares the eigenfrequencies obtained from the 2D and 3D problems. Growth rates in 2D and 3D are very similar, so the instability is largely associated with W_0. We thus expect the RWI to grow in 3D disks on the same timescales as in the razor-thin disks[5] (e.g., Li et al. 2000). The growth rate for the most unstable mode ($m = 3$) is only $\simeq 0.06\Omega_0$ but this corresponds to $\sim$3 orbits at r_0, so the instability operates on dynamical timescales.

Figure 2 compares the radial functions W_l for the $m = 3$ and $m = 5$ modes. In both cases, W_0 dominates over $W_{l>0}$, implying that the relative density perturbation is nearly z-independent. For $m = 3$, W_0 itself is dominated by the corotation region $r \sim r_0$, but for $m = 5$ the amplitude in the oscillatory region is larger than that around r_0. The $W_{l>2}$ modes are negligible, so 3D effects are due to W_2. Unlike W_0, in both cases $|W_2|$ has largest amplitudes in the wave-like regions toward the boundaries, and is smallest near r_0. This is consistent with the absorption of waves with $l > 0$ at corotation discussed in Li et al. (2003).

It is well known that in the razor-thin disk, as m is increased the RWI becomes more wave-like (as seen here for W_0) and is eventually quenched (Li et al. 2000). This might contribute to the slightly smaller growth rates obtained in the 3D problem than in the 2D problem (Table 1) since $W_{l>0}$ are wave-like (in addition to wave absorption at corotation). However, this effect is unimportant because their amplitudes are much smaller than W_0.

Although the observed stabilization effect increases with m, W_0 loses its RWI character at high m. Thus, it can be said that the RWI, considered as a low m, radially confined non-axisymmetric disturbance, has a growth rate determined by the 2D problem.

5.2. Flow in the (r, ϕ) Plane

Figure 3 shows the perturbed velocity field in the (r, ϕ) plane for the $m = 3$ mode above, and for a case with $\mathcal{A} = 1.6$ (growth rate $\sim 0.15\Omega_0$). The figure shows that anti-cyclonic motion at an overdensity is a robust feature. This confirms that the unstable modes found here are indeed the analog of the RWI in razor-thin disks. The perturbed horizontal velocity $(\delta v_r, \delta v_\phi)$ has negligible variation with respect to z.

[5] This statement assumes that the 2D problem gives similar growth rates to the equivalent razor-thin-disk setup, which we have checked to be the case.

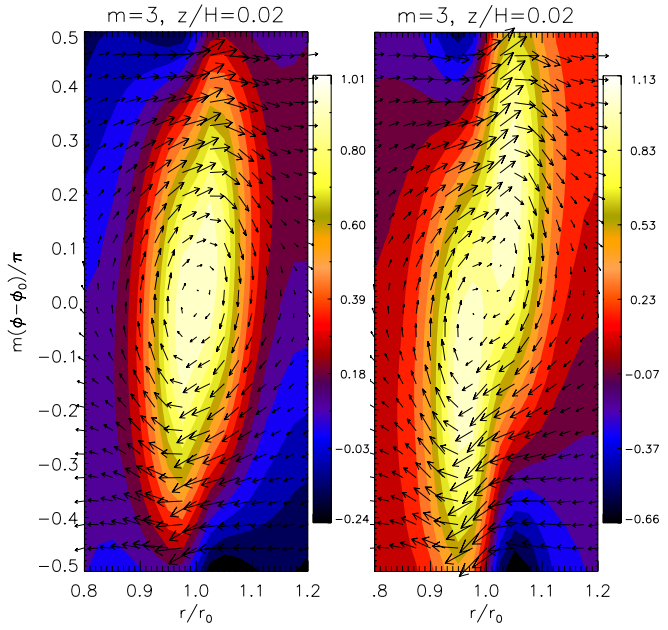

Figure 3. Perturbed horizontal velocity field in the (r, ϕ) plane, for the locally isothermal disk with $h = 0.07$ and $\mathcal{A} = 1.25$ (left) and with $\mathcal{A} = 1.6$ (right). The contours indicate relative density perturbation. The case with $\mathcal{A} = 1.6$ displays a double peak in density perturbation, which is explained in Li et al. (2000).

(A color version of this figure is available in the online journal.)

5.3. Vertical Flow

We now examine vertical flow associated with the RWI. We focus on the corotation region since this is where relative density perturbations are largest and vortex formation is expected.

Figure 4 shows the perturbed vertical velocity field in the (r, z) plane, at several azimuths. Since the largest contribution to δv_z comes from the $l = 2$ term in the expansion for W (Equation (32)), the magnitude of δv_z increases linearly with z.

Ahead of and behind the vortex core, the flow just follows the anti-cyclonic motion, with radial variations in δv_z being negligible. At $\phi = \phi_0$, there is also very little vertical motion for $z \lesssim 0.5H$, but there is upward motion at $r = 0.9,\ 1.1$, i.e., the edge of the vortex (see Figure 3). This can affect how dust particles are collected by RWI vortices.

For comparison, Figure 5 shows the vertical flow for the $m = 2$ mode. This flow is more two dimensional than the fiducial case above. This is expected for decreasing m (see, e.g., Papaloizou & Pringle 1985; Goldreich et al. 1986). It also appears qualitatively different (e.g., downward flow at $r = 1.1$ instead of upward as see for $m = 3$). We typically find locally isothermal disks to display a wider range of flow patterns around corotation than polytropic disks presented later, which show generic patterns.

Finally, Figure 6 shows the perturbed vertical velocity in the (ϕ, z) plane at $r = r_0$. Vertical motion is upward ahead of an anti-cyclonic vortex and downward behind it. The vertical velocity can be comparable to the perturbed azimuthal velocity, so the perturbed flow is fully three dimensional in this plane. However, the vortex center (r_0, ϕ_0) remains in vertical hydrostatic balance. This is not the case for polytropic disks.

5.4. Dependence of Vertical Flow on Instability Strength

We now assess how the three dimensionality of the flow in the corotation region varies with instability strength. We

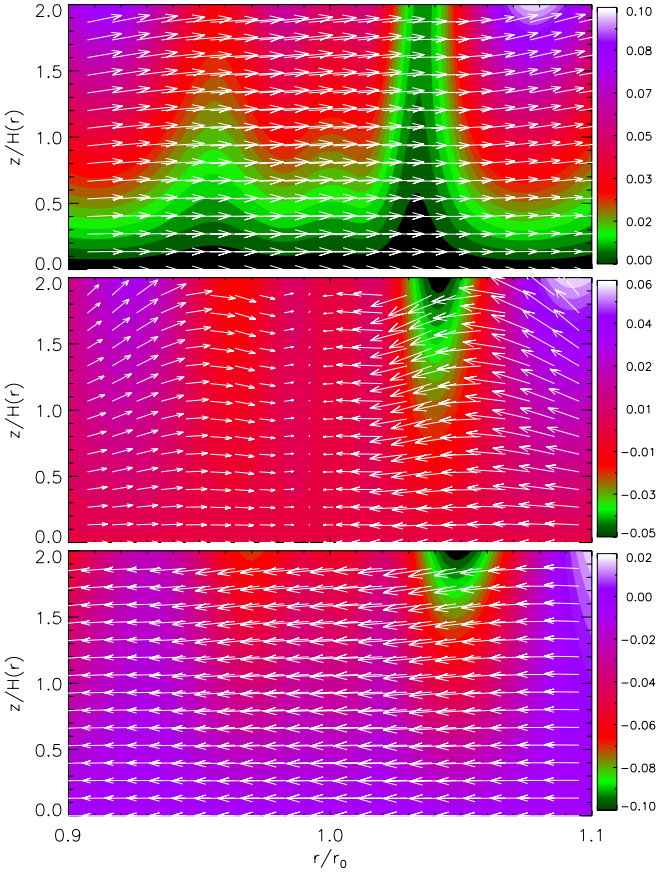

Figure 4. Vertical velocity field (contours) for the $m = 3$ mode in the locally isothermal disk with $h = 0.07$, in the (r, z) plane at azimuths $\theta \equiv m(\phi - \phi_0) = 0.2\pi$ (top), 0 (middle), and -0.2π (bottom). Arrows indicate the perturbed velocity field projected onto this plane.

(A color version of this figure is available in the online journal.)

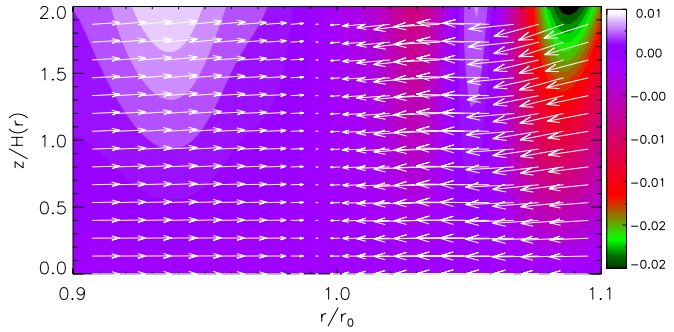

Figure 5. Vertical velocity field (contours) for the $m = 2$ mode in the locally isothermal disk with $h = 0.07$. The slice is taken at the azimuth $\phi = \phi_0$. This figure is to be compared with the middle plot in Figure 4. Arrows indicate the perturbed velocity field projected onto this plane.

(A color version of this figure is available in the online journal.)

examine the ratio $\langle|\delta v_z|\rangle/\langle|\delta v_r|\rangle$, where $\langle\cdot\rangle$ denotes averaging over $r \in [0.9, 1.1]$ and $z \in [0, 2H]$ at fixed azimuth $\phi = \phi_0$. In calculating this ratio, we ignore $W_{l>2}$ because the dominant contribution to δv_r and δv_z comes from W_0 and W_2, respectively. This ratio is large if there is significant vertical motion.

Results are shown in Figure 7, where the bump amplitude $\mathcal{A}$ is increased at fixed $h = 0.07$. Growth rates increase with $\mathcal{A}$, which is expected from previous works (Li et al. 2000), but the flow actually becomes *less* three dimensional with increasing instability strength.

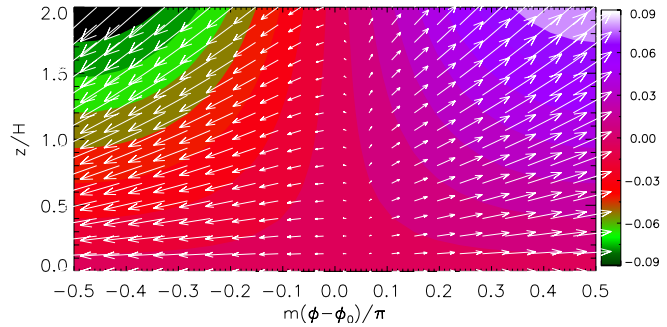

Figure 6. Vertical velocity field (contours) for the $m = 3$ mode in the locally isothermal disk with $h = 0.07$, in the (ϕ, z) plane at the radius $r = r_0$. Arrows indicate the perturbed velocity field projected onto this plane.

(A color version of this figure is available in the online journal.)

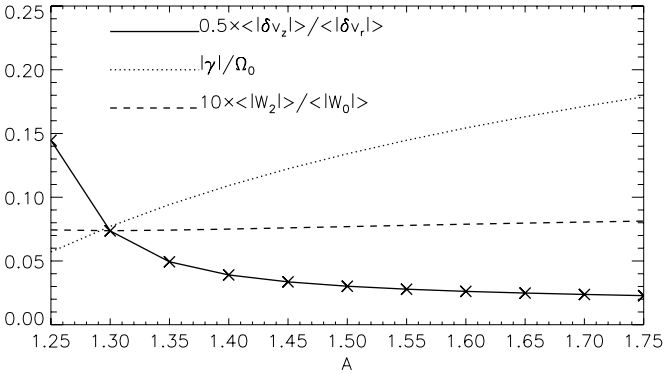

Figure 7. Average magnitude of vertical velocity (solid), in the corotation region of the RWI in the locally isothermal disk, as a function of bump amplitude $\mathcal{A}$ at fixed aspect ratio h. Also shown are the normalized amplitude of W_2 in this region (dashed) and the growth rates (dotted).

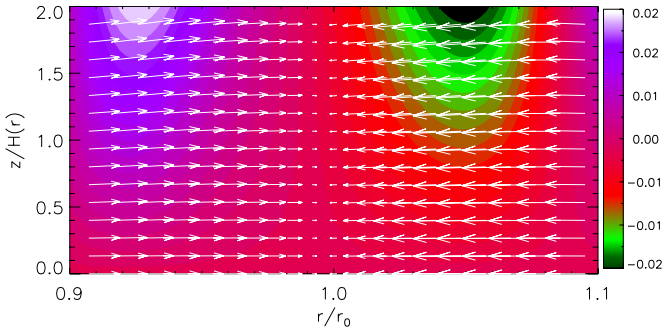

Figure 8. Same as Figure 4 but for a disk with $\mathcal{A} = 1.6$. The slice is taken at $\phi = \phi_0$.

(A color version of this figure is available in the online journal.)

In the corotation region where $\bar{\sigma} \sim i\gamma$, we expect from the linearized equation of motion that

$$|\delta v_z| \sim \frac{c_s^2}{H}\left|\frac{W_2}{\gamma}\mathcal{H}_2'\right|. \tag{45}$$

$|\delta v_z|$ scales with $1/|\gamma|$, so that increasing growth rates contributes to decreasing $|\delta v_z|$. Thus, the flow in the corotation region does not necessarily become more three dimensional with increasing $\mathcal{A}$.

It is clear from Figure 7 that three dimensionality decreases because of increasing $|\gamma|$ since $\langle|W_2|\rangle/\langle|W_0|\rangle$ varies weakly. We demonstrate this in Figure 8, which shows that in the disk with $\mathcal{A} = 1.6$ the flow is mainly horizontal. As in the fiducial case with $\mathcal{A} = 1.25$, there is little motion at $r = r_0$.

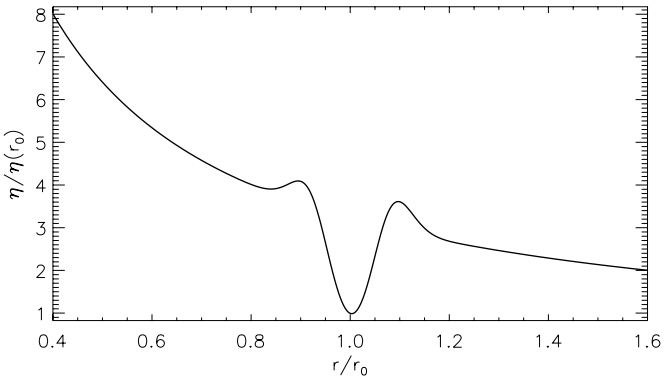

Figure 9. Background profile of the fiducial polytropic disk with $n = 1.5$, $\mathcal{A} = 1.4$, and $h = 0.14$ in terms of the vortensity.

Table 2
Eigenfrequencies in the $n = 1.5$ Polytropic Disk

m	$-\sigma_R/(m\Omega_0)$	$-10^2\gamma/\Omega_0$
1	0.9930 (0.9930)	4.4900 (4.4907)
2	0.9934 (0.9934)	8.2793 (8.2867)
3	0.9941 (0.9941)	10.769 (10.793)
4	0.9947 (0.9946)	11.594 (11.591)
5	0.9952 (0.9945)	10.646 (10.861)
6	0.9954 (0.9950)	8.0092 (8.5802)

Note. Values in brackets were obtained from the 2D problem.

Figures 7 and 8 shows that in the locally isothermal disk, more unstable modes are also more two dimensional (in the corotation region). $|W_2|$ remains a small fraction of $|W_0|$ and $|\delta v_z|$ is largely affected by $|\gamma|$.

However, $|\gamma|$ can be obtained by just solving the 2D problem. Thus, we could have anticipated the trend of $|\delta v_z|$ in Figure 7 based on only 2D calculations, with the assumption that changes in $|W_2|$ are less significant than the increase in $|\gamma|$. The above explicit calculation confirms this, suggesting we interpret the RWI as predominantly a 2D instability and that 3D effects on the RWI are small (for low m). We further illustrate these points with polytropic disks below.

6. RESULTS: POLYTROPIC DISKS

Our fiducial polytropic disk has polytropic index $n = 1.5$. In the absence of a bump, a surface density profile $\propto r^{-1/2}$ gives a constant aspect ratio ($H \propto r$). The bump parameters are set to $\mathcal{A} = 1.4$ and $h = 0.14$. Recall that for polytropic disks, H is the disk thickness and h is the aspect ratio at r_0.

Although the surface density enhancement is relatively large, it corresponds to only $\simeq$9% enhancement of the disk thickness at r_0. The background disk is shown in Figure 9 in terms of the vortensity profile. The fiducial disk has a global vortensity gradient ($\eta \propto r^{-1}$ away from r_0), but it is the local minimum that drives instability. The epicycle frequency is such that $\min(\kappa^2/\Omega_k^2) = 0.47$.

6.1. Solution Examples

Eigenfrequencies for the fiducial case are shown in Table 2. The modes of interest are those with disturbance amplitudes largest near r_0, which were found to correspond to $m \leqslant 4$. These modes have effectively the same growth rates in 2D and 3D. This gives confidence that the RWI is a 2D instability. We will consider $m = 3$ below in order to compare with locally

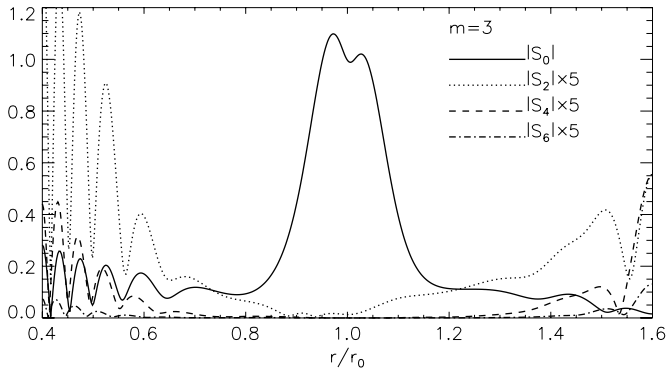

Figure 10. Radial functions S_l for the $n = 1.5$ fiducial polytropic disk. These are normalized by $|S_0(r_0)|$. The $l > 0$ modes have also been magnified in order to compare its radial structure with S_0.

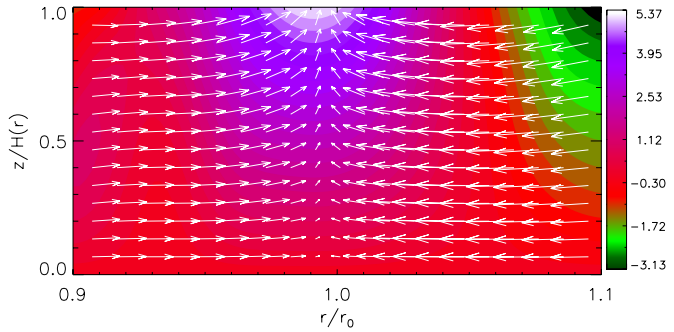

Figure 11. Vertical velocity field for the $m = 3$ mode in the $n = 1.5$ fiducial polytropic disk. The slice is taken in the (r, z) plane at the azimuth $\phi = \phi_0$. Arrows are the perturbed velocity field projected onto this plane.
(A color version of this figure is available in the online journal.)

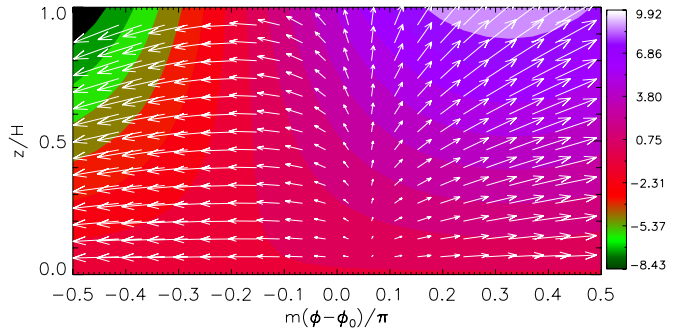

Figure 12. Vertical velocity field for the $m = 3$ mode in the $n = 1.5$ fiducial polytropic disk. The slice is taken in the (ϕ, z) plane at radius $r = r_0$. Arrows are the perturbed velocity field projected onto this plane.
(A color version of this figure is available in the online journal.)

isothermal disks. The $m = 3$ growth rate is only slightly smaller than the most unstable $m = 4$ mode. In corotation region, low m modes are also insensitive to radial boundary conditions (Lin & Papaloizou 2011a).

Figure 10 shows the S_l functions for the $m = 3$ case. These are similar to the locally isothermal disk (Figure 2). We typically find the $l > 0$ radial functions to have larger amplitudes (compared to $l = 0$) in the polytropic disk than in locally isothermal disks. $S_{l>0}$ have small but non-zero amplitudes near corotation, and their amplitude in the wave-like regions are at most $\simeq$20% of $|S_0(r_0)|$.

In the wave-like region, $|S_{l>0}|$ can be comparable to or larger than $|S_0|$. We found the solution in the wave regions more strongly affected by boundary conditions than in locally isothermal disks.

We remark that for $m = 5$, 6, S_0 no longer has the largest disturbance amplitude around r_0, because radial confinement around corotation requires low m (Lin & Papaloizou 2011a), unless the vortensity minimum is very deep. At sufficiently large m (which depends on parameters), the modes are dominated by the wave-like region (much like the $m = 5$ mode in locally isothermal disks; see Figure 2). Boundary conditions are likely to play a role here, but they are not the vortex-forming RWI modes of interest.

6.2. Vertical Structure

We now examine the $m = 3$ mode in more detail. The flow in the (r, ϕ) plane is similar to the locally isothermal disk. However, consistent with the previous section, vertical motion was found to be more prominent in the polytropic disk.

As before we focus on the region $r \in [0.9, 1.1]$. Figure 11 shows upward vertical motion at the vortex core and is largest near $z = H$. The flow for $z/H \lesssim 0.5$ and/or away from r_0 is essentially horizontal. The converging flow pattern in Figure 11 is consistent with (r_0, ϕ_0) being an overdensity. At the vortex core, upward motion makes sense since the midplane is reflecting. It also implies an increase in disk thickness at (r_0, ϕ_0).

The background polytropic disk becomes thicker at r_0 (i.e., H varies on a local scale). Fluid moving into the vortex core finds itself in a region of larger vertical extent. Upward motion enhances the disk thickness, consistent with enhanced pressure and with the RWI vortices being overpressure regions.

In the locally isothermal disk, it is difficult to directly associate vertical motion with enhanced pressure as above, since the scale height is prescribed to vary on a global scale and it remains unperturbed. Hence, vertical motion at (r_0, ϕ_0) was not seen in locally isothermal disks.

We have also examined the vertical flow in the polytropic disk for other m ($\leqslant$4), but found similar flow structure. This is unlike the locally isothermal disk, which can display a range of vertical flow pattern depending on m (Figures 4 and 5). This hints that there is a physical reason why polytropic disks tend to have positive vertical velocity at r_0. We return to this point later.

Lastly, Figure 12 shows the vertical flow in the (ϕ, z) plane at $r = r_0$. The flow is similar to that in the locally isothermal disk (Figure 6) except that the region $\phi \sim \phi_0$ is not in vertical hydrostatic equilibrium.

6.3. Effect of h and $\mathcal{A}$

We measure the three dimensionality of the flow in the corotation region in the same way as in Section 5.4, but here the averages are taken over the finite vertical extent of the disk.

Figures 13 and 14 show results from calculations with variable h (at fixed $\mathcal{A} = 1.4$) and variable $\mathcal{A}$ (at fixed $h = 0.14$), respectively. The range of growth rates is similar to the cases examined for the locally isothermal disk (see Figure 7). $|\gamma|$ and $\langle|X_2|\rangle$ also behave similarly.

As in locally isothermal disks, Figures 13 and 14 shows that the three dimensionality of the flow decreases with instability strength, but less rapidly in polytropic disks. Overall, $\langle|\delta v_z|\rangle/\langle|\delta v_r|\rangle$ does not vary much, consistent with our findings that the vertical flow structure, such as Figures 11 and 12, is generic. Such plots are qualitatively similar across the range

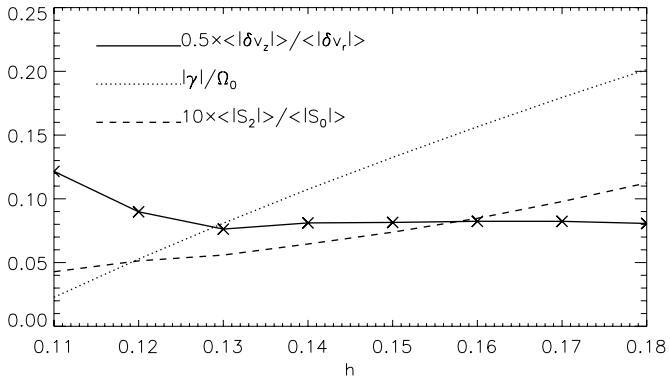

Figure 13. Effect of h on the three dimensionality of the corotation flow (solid). Also shown are the normalized amplitude of S_2 in this region (dashed) and the growth rates (dotted). The increase in growth rates with h is expected because the RWI is driven by pressure forces (Li et al. 2000).

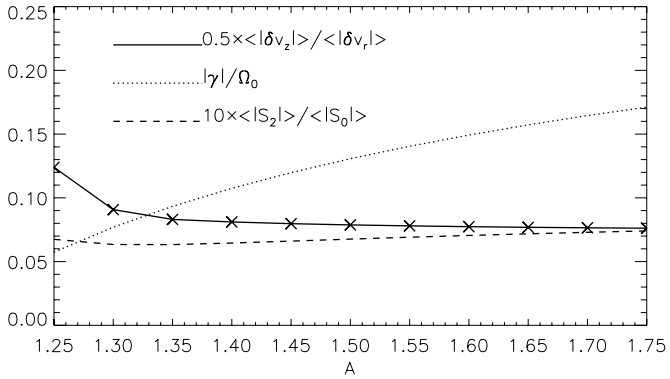

Figure 14. Same as Figure 13, but as a function of bump amplitude $\mathcal{A}$.

of h and $\mathcal{A}$ considered. The vertical flow at the vortex core is always upward.

When the spatial average is taken over $r \in [0.98, 1.02]$, we found $\langle \delta v_z \rangle / \langle |\delta v_r| \rangle$ maximizes at $h = 0.16$ for fixed $\mathcal{A}$ and at $\mathcal{A} = 1.6$ for fixed h. However, its values are of similar size: $\langle \delta v_z \rangle / \langle |\delta v_r| \rangle \simeq 0.44$–$0.65$ and $\langle \delta v_z \rangle / \langle |\delta v_r| \rangle \simeq 0.53$–$0.65$ for variable h and $\mathcal{A}$, respectively. A reason for such insensitivity is that the above calculations have fixed polytropic index n, thereby fixing the fluid properties. Below, we show that varying n affects the vertical flow.

6.4. Other Polytropic Indices

The polytropic index n not only affects the magnitude of the bump in the background disk thickness but also the compressibility of the fluid. An isothermal fluid can be considered a polytrope with $n \to \infty$ and is highly compressible, while $n = 0$ corresponds to an incompressible fluid. Thus, increasing n also increases compressibility.

For polytropic disks, we identified vertical flow at the vortex core. Here, we focus on this region and take radial averages over $r \in [0.98, 1.02]$. Figure 15 shows calculations for $n \in [1, 2.4]$. As n decreases, the instability strength increases and the vertical flow at r_0 noticeably increases, so the motion becomes more three dimensional. This is qualitatively different from varying h or $\mathcal{A}$, where the vertical flow at the vortex core remains of similar size.

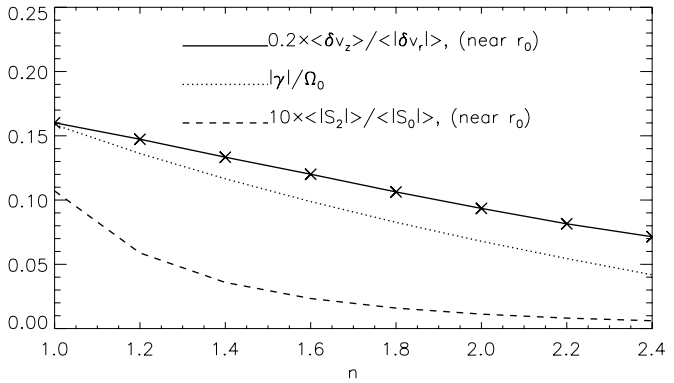

Figure 15. Dependence of the vertical flow at the vortex core on the polytropic index n (solid). The bump amplitude is fixed to $\mathcal{A} = 1.4$ and $h = 0.14$. Also shown are the growth rates (dotted) and amplitude of S_2 (dashed). The mode is $m = 3$.

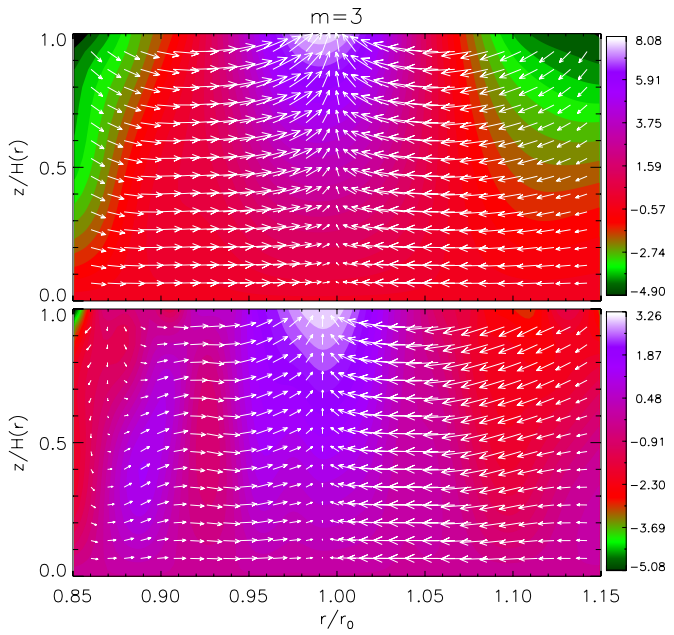

Figure 16. Comparison between vertical velocity (contour) in a disk with polytropic index $n = 1$ (top) and $n = 2$ (bottom). Arrows indicate the velocity field projected onto this plane.

(A color version of this figure is available in the online journal.)

At the corotation radius, which is close to r_0, the vertical velocity is

$$|\delta v_z| \sim \left| \frac{S_2}{\gamma H_0} \mathcal{C}_2^{\lambda'} \right| = \left| (4n^2 - 1) \frac{z S_2}{\gamma H_0^2} \right|. \quad (46)$$

H_0 is constant for fixed h. The factor $|(4n^2 - 1)/\gamma|$ decreases with decreasing n, which by itself would reduce the vertical velocity. Figure 15 shows this is not the case. The increase in $|S_2|$ with decreasing n overcomes this effect.

In Figure 16, we compare the flow in the (r, z) plane between $n = 1$ and $n = 2$. As previously noted, the flows share the same qualitative feature: converging toward r_0 with upward motion near r_0. However, for smaller n (stronger instability), upward motion is concentrated at r_0 whereas for larger n (weaker instability) there is also upward motion away from the vortex core. The latter was also seen for locally isothermal disks, consistent with larger n being more compressible.

A larger vertical velocity at r_0 with decreasing n is consistent with variable compressibility. First note that $|S_2| \ll |S_0|$ in $r \in [0.9, 1.1]$ so the perturbed enthalpy, and radial and azimuthal velocities are all dominated by S_0, which gives converging flow toward the vortex core where there is enhanced pressure or density. We may then ask what vertical motion at r_0 is compatible with this 2D perturbed flow, as implied by S_0?

At the vortex core (r_0, ϕ_0), the linearized continuity equation is approximately

$$\partial_t(\delta\rho/\rho) \sim -\nabla \cdot \delta \boldsymbol{v} - \delta v_z \partial_z \ln \rho,$$

where the δ quantities are regarded as real. If the fluid is highly compressible (large n), then the density at the vortex core may increase with vertical motion playing no role. That is, the divergence term on the right-hand side dominates over the second ($\nabla \cdot \delta \boldsymbol{v}$ itself is dominated by horizontal velocities).

However, if the fluid is made less compressible (decreasing n), so that $\nabla \cdot \delta \boldsymbol{v}$ is reduced in magnitude, then the fluid at (r_0, ϕ_0) should move upward so that $-\delta v_z \partial_z \ln \rho > 0$ contributes to increasing the density. For $n \ll 1$, the fluid becomes incompressible so that $\nabla \cdot \delta \boldsymbol{v}$ is negligible. Then the density can only increase with the fluid moving upward, increasing the disk thickness and accommodating more material.

It is important to note that in the above argument, we deduced vertical motion by imposing the 2D solution in the 3D disk. Effectively, we regarded S_0 as a source for S_2, and that S_2 has no back-reaction on S_0. This interpretation may not work for general disturbances, however. Here, it is justified by the fact that $|S_2| \ll |S_0|$ from the numerical calculations. Calculations where the disk is truncated by setting $r_i = 0.7$, $r_o = 1.3$, thereby excluding the wave-like regions in S_l, show similar upward motion. This indicates that S_0 induces S_2 locally.

7. DISKS WITH $\kappa^2 < 0$

Meheut et al. (2010) performed the first nonlinear hydrodynamic simulations that showed evidence for the RWI in a 3D polytropic disk. Their fiducial calculation showed the development of an $m = 1$ anti-cyclonic vortex which survived many orbits.

Indeed, the consideration of polytropic disks in this paper was originally inspired by these simulations, but it turns out that the disk model employed by Meheut et al. (2010) has a region where $\kappa^2 < 0$. Motivated by this feature, in this section we use Meheut et al.'s (2010) disk model to explore the 3D RWI when $\kappa_0^2 < 0$. We find that the RWI can be quite different from those described previously (where $\kappa^2 > 0$ everywhere).

It is straightforward to adapt our setups to models used by Meheut et al. They considered an $n = 1.5$ polytropic disk, occupying $r \in [r_i, r_o] = [1, 6]$, and specified the midplane density to be a power law ($\rho_0 \propto r^{-1/2}$) with a Gaussian bump. Their bump in midplane density has the same functional form as that used for the surface density in our models (Equation (5)), so $\mathcal{A}$ is now the bump amplitude in the midplane density. The bump is located at $r_0 = 3$ with width $\Delta r = 0.1 r_i$. The calculations presented below employed $N_r = 768$ grid points, on account of the larger disk compared to previous models.

We will consider the $m = 1$ mode below. Calculations were done for $m \leqslant 6$, which gave similar growth rates when $\kappa_0^2 < 0$, but provided $\mathcal{A}$ is chosen to ensure $\kappa_0^2 > 0$, then higher m modes become dominant (e.g., with $\mathcal{A} = 1.15$, $m = 5$ had the highest growth rate). The latter is qualitatively consistent with very recent numerical simulations (Meheut et al. 2012a; see also Appendix B.1).

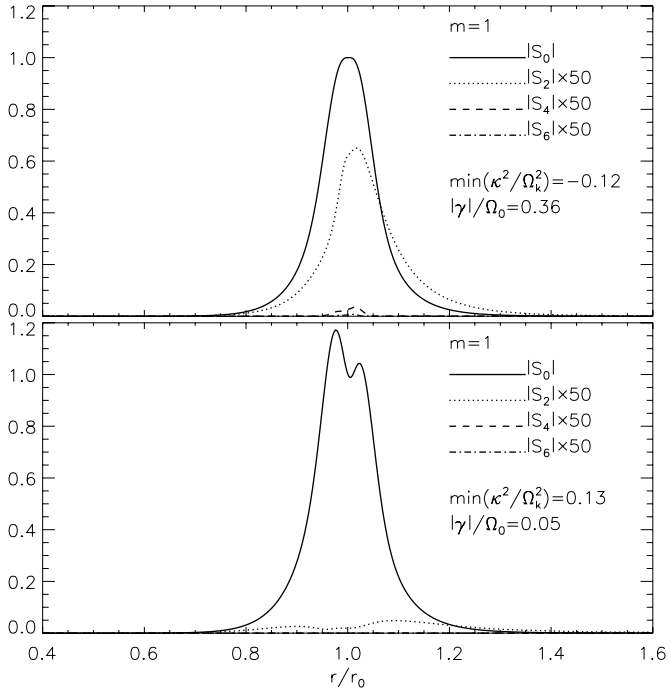

Figure 17. Radial functions S_l for the polytropic disk model with a bump in the midplane density of amplitude $\mathcal{A} = 1.4$ (top, Meheut et al.'s fiducial setup) and with a bump amplitude of $\mathcal{A} = 1.3$ (bottom). For $\mathcal{A} = 1.4$, $\kappa_0^2 < 0$.

When $\kappa_0^2 > 0$, we find similar flow structure to that described previously. Having applied the linear calculations to a different disk model and recovering similar results gives us confidence in the robustness of the RWI to develop 3D.

7.1. $m = 1$ Modes

In their fiducial setup, Meheut et al. adopted a bump amplitude of $\mathcal{A} = 1.4$. This results in $\kappa^2 = 0$ at $r \simeq 0.99 r_0$, $1.01 r_0$ and $\kappa_0^2 < 0$ (which is also reflected in their Figure 9). The disk is therefore unstable to local axisymmetric perturbations (Chandrasekhar 1961).

Interestingly, for $\mathcal{A} = 1.4$ we found an $m = 1$ mode with large growth rate, $|\gamma| = 0.36\Omega_0$, almost twice the largest growth rates found previously. Below, we examine this solution along with a case with $\mathcal{A} = 1.3$, which has $\kappa^2 > 0$ everywhere and growth rate $|\gamma| = 0.05\Omega_0$.[6]

Despite $\mathcal{A}$ being similar, the $m = 1$ growth rate for $\mathcal{A} = 1.3$ is much smaller than that for $\mathcal{A} = 1.4$. For $\mathcal{A} = 1.3$, we did not find other $m = 1$ modes with growth rates similar to the $m = 1$ mode in $\mathcal{A} = 1.4$. Furthermore, for $\mathcal{A} = 1.4$ the quantity $D = \kappa^2 - \tilde{\sigma}^2$ almost vanishes near r_0:

$$\min\left(|D|/\Omega_k^2\right) = 4 \times 10^{-3},$$

which occurs at $r = 1.002 r_0$. For $\mathcal{A} = 1.3$, the value above is 0.14.

Figure 17 compares the S_l functions for the cases above. While the double peak in S_0 for $\mathcal{A} = 1.3$ was also found in previous sections and also by Li et al. (2000), it is absent in $\mathcal{A} = 1.4$. The dominant 3D mode is S_2, but it is significantly larger in $\mathcal{A} = 1.4$ than in $\mathcal{A} = 1.3$. This indicates the vertical flow will also be qualitatively different.

[6] This is comparable to the nonlinear simulation.

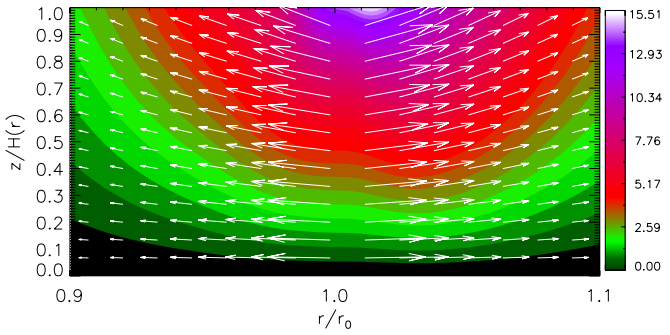

Figure 18. Vertical velocity field for an $m = 1$ mode in Meheut et al. (2010)'s disk model with $\mathcal{A} = 1.4$, which results in $\kappa^2 < 0$ at r_0 and $D \to 0$ there as well. The arrows are the perturbed velocity field projected onto this plane. This result is qualitatively different from modes with $\kappa^2 > 0$ (see figures in Section 6).

(A color version of this figure is available in the online journal.)

Figure 18 shows the flow pattern at $\phi = \phi_0$ for $\mathcal{A} = 1.4$. This result is very different from that for $\mathcal{A} = 1.3$, which share the same features as our previous setups with $\kappa^2 > 0$ (e.g., Figure 11). Note that while the S_l behave smoothly across r_0 (Figure 17), numerical evaluation of δv_r involves a division by D, which is very small near r_0 for $\mathcal{A} = 1.4$. Thus, horizontal velocities may be subject to numerical artifacts at r_0. Despite this, the direction of radial flow, being inward for $r < r_0$ and outward for $r > r_0$ with a sharp transition at r_0, was also found in Meheut et al. (2010, their Figure 11).

$\mathcal{A}$ also did not produce vertical flow consistent with that in Meheut et al. (2010) where strong downward flow at r_0 was identified with rolls excited on either side. By contrast the linear solutions have upward motion and there is no vertical motion in the (r, z) plane.

Despite using the same disk models, several factors may have contributed to the discrepancy between the linear calculation above and Meheut et al.'s simulation. These include the treatment of the vertical domain, nonlinearities (H. Meheut 2012, private communication) and interaction with other m modes in the simulation which cannot be treated in linear theory.

There may also be numerical issues in our linear calculation because of $\kappa^2 \leqslant 0$. The RWI is associated with the term $\propto (1/\bar{\sigma})\partial_r(\rho_0\Omega/D)$ and its disturbance is localized about r_0. This term is $\propto 1/\kappa^2$, which diverges when $\kappa^2 \to 0$ near r_0. Also, because $\kappa_0^2 < 0$, it allows $D \to 0$ at corotation as well. We have performed calculations with lower spatial resolution, so that numerically κ^2 and D have larger deviations from zero, but we found eigenfrequencies and flow patterns similar to the case shown above. We will further comment on RWI modes with $\kappa_0^2 < 0$ in Section 8.3.

8. SUMMARY AND DISCUSSION

In this paper, we have examined the linear stability of three-dimensional, vertically stratified and radially structured disks. Our calculations are 3D analogs of those presented by Li et al. (2000), in which the RWI was studied in razor-thin disks. In order to simplify the problem, we assumed the perturbed hydrodynamic quantities have vertical dependence that can be decomposed into Hermite or Gegenbauer polynomials. Our conclusions therefore apply to such perturbations only.

Our numerical calculations confirm the RWI persists in 3D. For ease of discussion below, we denote the full linear solution schematically as

$$X = Y(r) + \Delta Y(r, z),$$

where Y is the z-independent part of the solution and ΔY is the part that also depends on z.

8.1. Validity of 2D

We find that the RWI growth rate $|\gamma|$ can be accurately determined from the 2D problem alone. In other words, instability is associated with $Y(r)$. In the region of interest—the vortensity minimum—where vortex formation is expected, we find $|\Delta Y| \ll |Y|$ so that enthalpy, radial velocity, and azimuthal velocity perturbations have essentially no z-dependence.

In fact, weak z-dependence is expected from earlier studies of accretion tori. For slender tori, Papaloizou & Pringle (1985) demonstrated the existence of low m unstable modes with weak z-dependence. Goldreich et al. (1986) also justified the use of height-averaged equations for calculating modes in narrow tori, for which vertical hydrostatic equilibrium was assumed. Although we considered radially extended disks, their results should apply here because the low m RWI modes, relevant to vortex formation, have the largest disturbance associated with a narrow region about the density bump. More recently, Umurhan (2010) reproduced the RWI in approximate 3D disk models, in which horizontal velocities have no vertical dependence. Our numerical results are therefore supported by analytic studies above.

The 2D solution, Y, implies anti-cyclonic motion associated with overdensities, thus we expect the RWI will lead to columnar vortices in 3D. The survival of vortices in 3D is then an important issue because they may be subject to instabilities (Lesur & Papaloizou 2009, 2010). On the other hand, if there is a continuous source of vortensity extremum, such as disk–planet interaction, then vortex formation via the RWI could be maintained.

8.2. Vertical Motion

Although $|\Delta Y|$ is small in the corotation region, it is nevertheless non-zero. This implies vertical motion growing on dynamical timescales, making the flow in the corotation region three dimensional. We found the nature of the vertical flow is affected by the EOS.

In polytropic disks, the vortex core (r_0, ϕ_0) always involves upward motion. For a fixed polytropic index n, there is limited variation in the magnitude of vertical flow with respect to instability strength. However, if the fluid is made less compressible by lowering n, then vertical motion at the vortex core increases.

This result motivates us to interpret vertical motion around corotation as a perturbation to the 2D solution (Goldreich et al. 1986). Recall that Y is the solution to the vertically integrated system. It signifies non-axisymmetric enhancements in surface density at the bump radius. This characteristic feature is unchanged by the addition of ΔY to the 2D solution. We then ask how the disk should respond in the vertical direction.

The polytropic disk thickness is directly related to the surface density (Equation (12)). Enhancement of the surface density therefore implies enhancement in disk thickness, so fluid at (r_0, ϕ_0) moves upward. If we look in the (ϕ, z) plane at r_0, the disk thickness becomes non-axisymmetric. This has already been observed in nonlinear simulations (Meheut et al. 2011a, 2011b). In these newer simulations, the authors indeed find upward motion in anti-cyclonic vortices.

Note that the polytropic disk thickness becomes less sensitive to surface density as n is increased (Equation (12)). For $n \to \infty$, the disk thickness is independent of surface density and there is no need for fluid to move vertically in order to achieve a surface density increase. In this case, there is no preference for vertical velocity of a particular sign at (r_0, ϕ_0). Since the fluid behaves isothermally as $n \to \infty$, the above is consistent with our observation that locally isothermal disks have little vertical motion right at the vortex core. In Appendix B.2, we consider a polytropic disk calculation with $n = 8$ to check for consistency.

8.3. RWI with $\kappa^2 < 0$

We briefly examined the linear 3D RWI in disk where κ^2 becomes negative at the density bump. This was inspired by the 3D RWI simulations presented in Meheut et al. (2010), where the disk model had $\kappa_0^2 < 0$. In this setup, we found an $m = 1$ linear mode with large growth rate and qualitatively different from modes in disks with $\kappa^2 > 0$ everywhere. In neither case did we reproduce the vertical flow seen in Meheut et al. (2010), namely, downward flow at the vortex center.

Most discussions of non-axisymmetric disk instabilities have assumed $\kappa^2 > 0$ everywhere, including Lovelace et al.'s (1999) original description of the RWI, so that Rayleigh's criterion for stability against local axisymmetric perturbations is satisfied.

The RWI has been shown to exist for $\kappa_0^2 < 0$ but its properties appear different from those in disks with $\kappa_0^2 > 0$. For example, Li et al.'s (2000) linear calculations indicate a non-smooth change in growth rate as κ_0^2 becomes negative (the "homentropic Gaussian bump (HGB)" case in their Figure 9). In nonlinear 2D simulations by Li et al. (2001), the RWI also evolves differently depending on whether the growth rate is low ($|\gamma| \sim 0.1\Omega_0$ and $\kappa_0^2 > 0$) or high ($|\gamma| \sim 0.3\Omega_0$ and $\kappa_0^2 < 0$). Note that the latter case has $|\gamma|$ close to that found in our calculation. We therefore expect the RWI to differ in 3D depending on $\mathrm{sgn}(\kappa_0^2)$. This is apparent by comparing our results with $\kappa_0^2 > 0$ to those with $\kappa_0^2 < 0$.

Thus, while Meheut et al. (2010) is the first demonstration of the 3D RWI, it should be kept in mind that the disk model has $\kappa_0^2 < 0$. An understanding of such modes in 3D is of theoretical interest, but it is unclear whether or not protoplanetary disks will develop sufficiently large pressure gradients to render $\kappa^2 < 0$ (Yang & Menou 2010).

8.4. Outstanding Issues

The main goal of our study is to demonstrate the linear RWI in 3D and to identify the nature of associated 3D flow structure around corotation. However, our study is subject to several caveats which should be clarified in future work.

8.4.1. Baroclinic Effects

One issue is that our locally isothermal basic states are not in true equilibrium, because we approximated the rotation profile to be z-independent (Equation (8)). Initializing a full hydrodynamic simulation this way might boost radial velocities because of the inexact radial momentum balance. In order for the angular velocity to be strictly independent of z, we must set $H \propto r^{3/2}$, which is the globally isothermal disk already considered by Meheut et al. (2012b). We do not expect this to make a difference from our disks with $H \propto r$, because the RWI is driven by local variations in disk structure and its disturbance is radially confined. We check this in Appendix B.2.

Another justification is that for a thin, smooth disk ($\mathcal{A} = 1$) with $H = hr$, the angular velocity is

$$\Omega(r, z) = \Omega_k \left[1 - \frac{h^2}{2} \left(\alpha + 2 + \frac{z^2}{2H^2} \right) \right] \tag{47}$$

(Tanaka et al. 2002). The difference in angular speed between the gas at the midplane and gas at z is then

$$\Delta\Omega \equiv |\Omega(r, z) - \Omega(r, 0)| = h^2 \left(\frac{z^2}{4H^2} \right) \Omega_k \tag{48}$$

(a radial density bump does not contribute to this difference). Since the gas is contained within a few scale heights, we have $\Delta\Omega/\Omega_k = O(h^2)$. Because $h \ll 1$, vertical shear should be unimportant if the dynamics of interest operate on much faster timescales, as can be the case for the RWI with growth rates $\sim h\Omega_k$. That is, the vortical perturbation grows much faster than it is sheared apart by $\Delta\Omega$. We have begun preliminary nonlinear simulations which confirms vortex formation via the RWI in a locally isothermal 3D disk with constant aspect ratio (Lin 2012).

Knobloch & Spruit (1986) have pointed out the possibility of baroclinic instability in the case of $\Omega = \Omega(r, z)$, when there are radial variations in temperature on the scale of local scale heights. This condition is not met in our locally isothermal disk models because the sound speed varies on a global scale. In more realistic disk models, one might expect that a density bump also involves local temperature variations. Baroclinic effects may then become important. On the other hand, the RWI may also be enhanced because of local temperature gradients (Li et al. 2000). Having $\Omega = \Omega(r, z)$ means solving the linearized equations as a PDE eigenvalue problem, which is not simple.

8.4.2. Boundary Effects

We have restricted our attention to the corotation region because this is where vortex formation eventually takes place. Distant radial boundaries do not affect the dynamics in this region significantly (as checked numerically). However, it is clear that far away from corotation, 3D effects become increasingly important. This is seen in the polytropic disk as $|\Delta Y| \sim |Y|$ toward the disk boundaries (Figure 10). Disturbances associated with the RWI are therefore three dimensional beyond the Lindblad resonances. In order to study these regions, more physically realistic radial boundary conditions are needed.

Around corotation, the RWI is a global disturbance in z, so the upper disk boundary conditions could be important. The use of orthogonal polynomials means we simply impose a regularity condition at the upper disk boundary (Section 4). This solution method does not allow us to explore the effect of other vertical boundary conditions. Again, such a study involves a PDE eigenvalue problem, but can reveal to what extent the dominance of the 2D solutions found here are influenced by the specific decompositions employed. This will be the subject of a follow-up paper.

Nevertheless, we can make some speculations based on results here. The vanishing density at the polytropic disk surface is likely to provide a reflective upper boundary. This effect may be important. It might reduce the growth of the RWI if it remains predominantly a 2D disturbance, because the 2D solution alters the surface density, which is directly related to the disk thickness for a polytrope, but the disk thickness cannot change.

I thank H. Meheut for useful discussions and clarification of their simulation results. I also thank O. Umurhan for comments on the first version of this paper.

APPENDIX A

EXPLICIT EXPRESSIONS FOR THE LINEAR OPERATORS

A.1. Locally Isothermal Disks with Constant Aspect Ratio

For locally isothermal disks with $H = hr$ with h being a constant and Ω taken to be a function of radius only, the operators governing the linear problem are given by

$$A_l = \left[\frac{2mr\Omega}{\bar{\sigma}}\frac{d}{dr}\ln\left(\frac{c_s^2\Sigma\Omega}{D}\right) - \left(m^2 + \frac{r^2 D}{c_s^2}\right) + \frac{lD}{\bar{\sigma}^2 h^2} - lr\frac{d}{dr}\ln\left(\frac{c_s^2\Sigma}{D}\right) - l(2l-1) + \frac{4m\Omega l}{\bar{\sigma}}\right] + r^2\frac{d}{dr}\left[\ln\left(\frac{rc_s^2\Sigma}{D}\right)\right]\frac{d}{dr} + r^2\frac{d^2}{dr^2}, \quad \text{(A1)}$$

$$B_l = -\left[(l-2) - \frac{2m\Omega}{\bar{\sigma}}\right] + r\frac{d}{dr}, \quad \text{(A2)}$$

$$C_l = -(l+1)(l+2)\left[r\frac{d}{dr}\ln\left(\frac{c_s^2\Sigma}{D}\right) + l - \frac{2m\Omega}{\bar{\sigma}}\right] - r(l+1)(l+2)\frac{d}{dr}. \quad \text{(A3)}$$

We have expressed the operators in terms of surface density Σ so the above may be seen to be equivalent to Equation (21) in Tanaka et al. (2002) when their parameter $\mu = d\ln H/d\ln r$ is set to unity.

These equations are approximate because we ignored terms proportional to $\partial_z\Omega$ in the governing PDE from which Equations (A1)–(A3) are derived. These terms are non-vanishing for exact equilibrium if the sound speed varies with radius, but for a thin disk $\partial_z\Omega \propto h^2 \ll 1$ so we expect them to be small. It is worth neglecting them in favor of the one-dimensional operators above, which are much simpler. Tanaka et al. (2002) give a more general equation for the linear problem which includes $\partial_z\Omega$. Their Equation (11) shows that $\partial_z\Omega$ contributes to the coefficient of $\partial_z W$ as

$$\frac{\partial W}{\partial z}\left[\frac{z}{H^2} + \frac{m}{\bar{\sigma}}\frac{\partial\Omega}{\partial z}\right] = \frac{z}{H^2}\frac{\partial W}{\partial z}\left[1 - \frac{mh^2 q\Omega_k}{\bar{\sigma}}\right], \quad \text{(A4)}$$

where $\partial_z\Omega$ is evaluated using Tanaka et al.'s Equation (4) and $q \equiv -d\ln c_s/d\ln r = 0.5$ for disks with constant aspect ratio (equivalent to Equation (48) in Section 8.4.1). Near corotation the magnitude of the second to first term is

$$\left|mh^2 q\frac{\Omega_k}{\bar{\sigma}}\right| \sim \frac{mh^2 q}{|\gamma/\Omega_k|}. \quad \text{(A5)}$$

For the fiducial case in Section 5, $m = 3$, $h = 0.07$, and $|\gamma/\Omega_k| \simeq 0.057$, this ratio is 0.13. We typically find $|\gamma/\Omega_k| = O(h)$, so the second term is a factor $mhq \ll 1$ smaller than the first for low m modes. Neglecting it (to arrive at Equations (A1)–(A3)) is a self-consistent treatment.

A.2. Polytropic Disks

For polytropic disks, we find it most convenient to express the linear operators as

$$A_0 = -\mathcal{V}^{(1)} + \frac{(2\lambda+1)}{2(\lambda+1)}[\mathcal{V}^{(2)} - \mathcal{V}^{(4)} + \mathcal{V}^{(6)} - \mathcal{V}^{(7)} + \mathcal{V}^{(8)}], \quad \text{(A6)}$$

$$A_{l>0} = -\mathcal{V}^{(1)} + \frac{1}{2(l+\lambda+1)(l+\lambda-1)} \times \{(l^2+2\lambda l+2\lambda^2-\lambda-1)[\mathcal{V}^{(2)}+\mathcal{V}^{(6)}+\mathcal{V}^{(8)}] + l(l+2\lambda)[\lambda\mathcal{V}^{(3)} - (l^2+2\lambda l-1)\mathcal{V}^{(5)}] - [(\lambda+1)l^2 + 2\lambda(\lambda+1)l + 2\lambda^2 - \lambda - 1]\mathcal{V}^{(4)} - (l^2+2\lambda l+\lambda-1)(2\lambda+1)\mathcal{V}^{(7)}\} - l(l+2\lambda)\mathcal{V}^{(9)}, \quad \text{(A7)}$$

$$B_l = -\frac{l(l-1)}{4(l+\lambda-2)(l+\lambda-1)}\{\mathcal{V}^{(2)} + (l-2)\mathcal{V}^{(3)} + (l+2\lambda-1)[\mathcal{V}^{(4)} + (l-2)\mathcal{V}^{(5)}] + \mathcal{V}^{(6)} + (2\lambda+1)\mathcal{V}^{(7)} + \mathcal{V}^{(8)}\}, \quad \text{(A8)}$$

$$C_l = \frac{(l+2\lambda+1)(l+2\lambda)}{4(l+\lambda+1)(l+\lambda+2)}\{-\mathcal{V}^{(2)} + (l+2\lambda+2)\mathcal{V}^{(3)} + (l+1)[\mathcal{V}^{(4)} - (l+2\lambda+2)\mathcal{V}^{(5)}] - \mathcal{V}^{(6)} - (2\lambda+1)\mathcal{V}^{(7)} - \mathcal{V}^{(8)}\}, \quad \text{(A9)}$$

where

$$\mathcal{V}^{(1)} = \frac{nD\rho_0^{-1/n}r^2}{K(1+n)}, \quad \mathcal{V}^{(2)} = r^2\left\{\frac{d}{dr}\left[\ln\left(\frac{\rho_0 r}{D}\right)\right]\frac{d}{dr} + \frac{d^2}{dr^2}\right\},$$
$$\mathcal{V}^{(3)} = -r^2\left\{\frac{H'}{H}\frac{d}{dr}\left[\ln\left(\frac{\rho_0 r}{D}\right)\right] + \left(\frac{H'}{H}\right)' + \frac{H'}{H}\frac{d}{dr}\right\},$$
$$\mathcal{V}^{(4)} = -r^2\frac{H'}{H}\frac{d}{dr}, \quad \mathcal{V}^{(5)} = r^2\left(\frac{H'}{H}\right)^2,$$
$$\mathcal{V}^{(6)} = \frac{2mr\Omega}{\bar{\sigma}}\frac{d}{dr}\left[\ln\left(\frac{\rho_0\Omega}{D}\right)\right],$$
$$\mathcal{V}^{(7)} = -\frac{2mr\Omega}{\bar{\sigma}}\left(\frac{H'}{H}\right), \quad \mathcal{V}^{(8)} = -m^2,$$
$$\mathcal{V}^{(9)} = -\frac{r^2 D}{\bar{\sigma}^2 H^2}. \quad \text{(A10)}$$

We have used the midplane density ρ_0, but it is straightforward to express the above in terms of Σ using the relation $\Sigma = \rho_0 H(r) I_n$. The form of the operators above is appropriate for numerical computations in the range of polytropic indices considered in this paper ($n \geqslant 1$ or $\lambda \geqslant 0.5$). Numerical issues may arise for smaller indices because of the $(l+\lambda-2)^{-1}$ factor in B_l. For example, if $\lambda = 0$ ($n = 0.5$) and $l = 2$ this factor diverges. However, for $n = 0.5$ it is more natural to use Chebyshev polynomials of the first kind (T_l) for expansion in $\hat{z}$. We have performed calculations with $n = 0.5$ using T_l, and found similar results to those presented here.

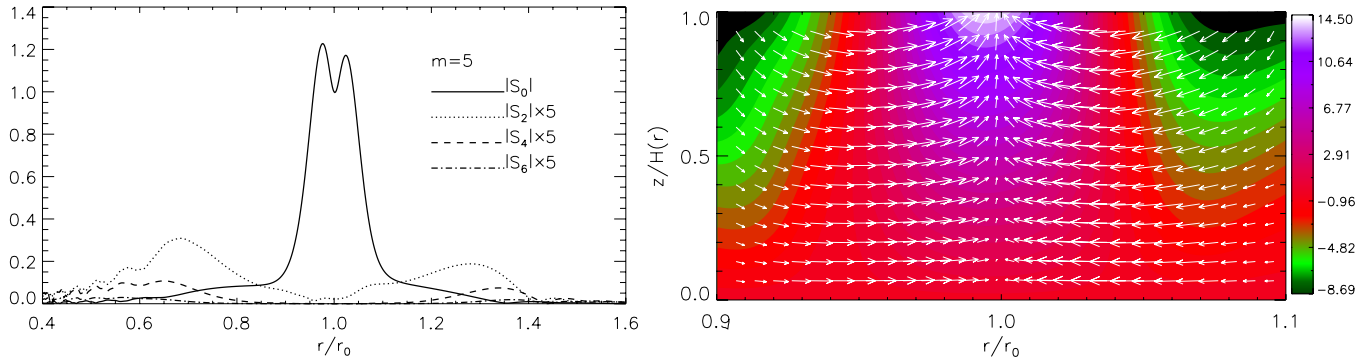

Figure 19. Linear $m = 5$ mode found in Meheut et al.'s (2012a) $n = 1.5$ polytropic disk model, but with a smaller bump amplitude than their simulation. Left: radial eigenfunctions S_l normalized by $|S_0(r_0)|$. Right: vertical flow structure.

(A color version of this figure is available in the online journal.)

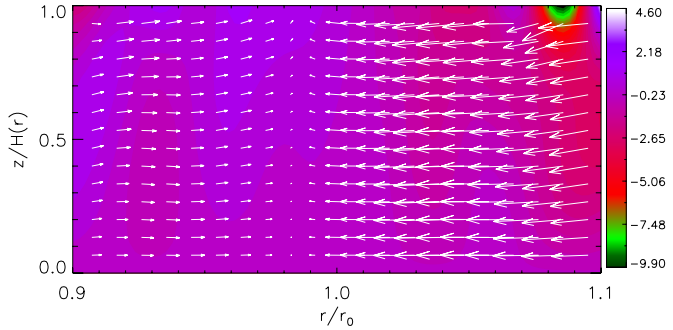

Figure 20. $m = 3$ mode in the standard $n = 8$ polytropic disk (growth rate $|\gamma| = 0.055\Omega_0$). Contours of the real vertical velocity perturbation are shown. Arrows are the perturbed velocity field projected onto this plane. This figure is similar to locally isothermal disks in that there is very little vertical velocity near the vortex core, and is unlike polytropic disks with smaller n (e.g., Figure 16, which shows significant upward motion near $r = r_0$).

(A color version of this figure is available in the online journal.)

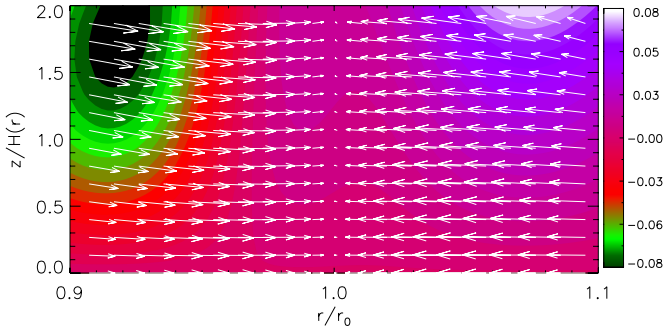

Figure 21. Linear mode in the locally isothermal disk with the same parameter values as the Meheut et al.'s (2012b) globally isothermal disk ($m = 4$, $h = 0.1$, other parameters are the same as our fiducial case in Section 5). Contours of the real vertical velocity perturbation are shown. Arrows are the perturbed velocity field projected onto this plane. The growth rate $|\gamma| = 0.20\Omega_0$ is similar to Meheut et al. The vertical flow is also consistent with their Figure 3(d), namely, the vertical velocity vanishes near $r = r_0$.

(A color version of this figure is available in the online journal.)

APPENDIX B

SUPPLEMENTARY CALCULATIONS

B.1. Improved Simulations

During the finishing stages of this paper, Meheut et al. (2012a) published new simulations of the 3D RWI with improved numerical resolution. This simulation developed an $m = 5$ mode with growth rate $|\gamma| = 0.17\Omega_0$, with upward motion at anti-cyclonic vortex centers and downward motion at cyclonic vortex centers, which are consistent with our fiducial polytropic disks (Section 6).

We were able to find an $m = 5$ linear mode provided the bump amplitude $\mathcal{A}$ in the midplane density was chosen to ensure $\kappa^2 > 0$. Using $\mathcal{A} = 1.7$, we find $|\gamma| = 0.18\Omega_0$ for $m = 5$. This mode is shown in Figure 19. Note that S_0 is still localized about r_0, despite the higher m than those considered in our fiducial calculations (which gave more global disturbances). This is because here the vortensity minimum is deep, with $\min(\kappa^2/\Omega_k^2) \simeq 0.1$, so even high m modes can be localized. The vertical flow at the vortex core is upward, as found previously.

Meheut et al. (2012a) actually employed $\mathcal{A} = 2$, giving $\kappa_0^2 \simeq -0.2\Omega_k^2$, for which we were unable to find a linear mode with similar growth rate as their simulation. As κ_0^2 is more negative in their new simulation than in Meheut et al. (2010), one possibility is that an axisymmetric disturbance develops early on, rendering $\kappa^2 \gtrsim 0$ then the usual RWI follows. For $\mathcal{A} = 1.7$, we find linear growth rates peak at $m = 8$ with $|\gamma| = 0.21\Omega_0$, but this is only marginally larger than $m = 5$. Differences in the linear and nonlinear calculations, such as the treatment of vertical boundaries, may then account for observation of $m = 5$ in the simulations.

B.2. Consistency Check

We describe calculations to check the consistency between locally isothermal and polytropic disks and against the globally isothermal disk presented in Meheut et al. (2012b).

Noting that an isothermal disk is a special case of a polytropic disk in the limit of large n, we performed a polytropic disk calculation with $n = 8$, $\mathcal{A} = 2.0$, and $h = 0.2$. Figure 20 shows that in this case, vertical motion is much smaller than the horizontal flow in the corotation region, compared to smaller values of n discussed in Section 6.4. This is consistent with our typical results for locally isothermal disks where the vertical velocity vanishes at the vortex core.

Meheut et al. (2012b) solved the linear problem for globally isothermal disks. Their basic state with $\Omega = \Omega(r)$ satisfies exact radial momentum balance but adopting such a profile for locally isothermal disks is only approximate. We have performed a locally isothermal calculation with the same parameters as Meheut et al. (2012b). The result is shown in Figure 21. It shares the same vertical flow implied by Meheut et al.'s (2012b) Figure 3(d) around a maximum in the (real) density perturbation:

$\delta v_z > 0$ near $r = 1.1$, $\delta v_z < 0$ near $r = 0.9$, and $\delta v_z \sim 0$ at $r = r_0$. This suggests that a node in the vertical velocity at the vortex core is a generic feature for linear RWI modes in isothermal disks. A global temperature profile does not affect the 3D RWI significantly.

REFERENCES

Abramowitz, M., & Stegun, I. A. (ed.) 1965, Handbook of Mathematical Functions with Formulas, Graphs, and Mathematical Tables (New York: Dover Publications)
Armitage, P. J. 2011, ARA&A, 49, 195
Balbus, S. A., & Hawley, J. F. 1991, ApJ, 376, 214
Barge, P., & Sommeria, J. 1995, A&A, 295, L1
Chandrasekhar, S. (ed.) 1961, Hydrodynamic and Hydromagnetic Stability (Oxford: Oxford Univ. Press)
Crespe, E., Gonzalez, J.-F., & Arena, S. E. 2011, in SF2A-2011: Proc. Annual Meeting of the French Society of Astronomy and Astrophysics, ed. G. Alecian, K. Belkacem, R. Samadi, & D. Valls-Gabaud, 469 (http://sf2a.cesr.fr/php/spip/spip.php?article350)
de Val-Borro, M., Artymowicz, P., D'Angelo, G., & Peplinski, A. 2007, A&A, 471, 1043
Dong, R., Rafikov, R. R., & Stone, J. M. 2011, ApJ, 741, 57
Gammie, C. F. 1996, ApJ, 457, 355
Goldreich, P., Goodman, J., & Narayan, R. 1986, MNRAS, 221, 339
Goldreich, P., & Tremaine, S. 1979, ApJ, 233, 857
Goldreich, P., & Tremaine, S. 1980, ApJ, 241, 425
Knobloch, E., & Spruit, H. C. 1986, A&A, 166, 359
Koller, J., Li, H., & Lin, D. N. C. 2003, ApJ, 596, L91
Lesur, G., & Papaloizou, J. C. B. 2009, A&A, 498, 1
Lesur, G., & Papaloizou, J. C. B. 2010, A&A, 513, A60
Li, H., Colgate, S. A., Wendroff, B., & Liska, R. 2001, ApJ, 551, 874
Li, H., Finn, J. M., Lovelace, R. V. E., & Colgate, S. A. 2000, ApJ, 533, 1023
Li, H., Li, S., Koller, J., et al. 2005, ApJ, 624, 1003
Li, H., Lubow, S. H., Li, S., & Lin, D. N. C. 2009, ApJ, 690, L52
Li, L.-X., Goodman, J., & Narayan, R. 2003, ApJ, 593, 980
Lin, D. N. C., & Papaloizou, J. 1986, ApJ, 309, 846
Lin, M.-K. 2012, MNRAS, submitted (arXiv:1205.4034)
Lin, M.-K., & Papaloizou, J. C. B. 2010, MNRAS, 405, 1473
Lin, M.-K., & Papaloizou, J. C. B. 2011a, MNRAS, 415, 1426
Lin, M.-K., & Papaloizou, J. C. B. 2011b, MNRAS, 415, 1445
Lovelace, R. V. E., Li, H., Colgate, S. A., & Nelson, A. F. 1999, ApJ, 513, 805
Lyra, W., Johansen, A., Klahr, H., & Piskunov, N. 2008, A&A, 491, L41
Lyra, W., Johansen, A., Zsom, A., Klahr, H., & Piskunov, N. 2009, A&A, 497, 869
Meheut, H., Casse, F., Varniere, P., & Tagger, M. 2010, A&A, 516, A31
Meheut, H., Keppens, R., Casse, F., & Benz, W. 2012a, A&A, 542, 9
Meheut, H., Varniere, P., & Benz, W. 2011a, in EPSC-DPS Joint Meeting 2011, 2–7 October 2011, Nantes, France, 1054
Meheut, H., Varniere, P., Casse, F., & Tagger, M. 2011b, in EPSC-DPS Joint Meeting 2011, 2–7 October 2011, Nantes, France, 1059
Meheut, H., Yu, C., & Lai, D. 2012b, MNRAS, 422, 2399
Muto, T., Suzuki, T. K., & Inutsuka, S.-I. 2010, ApJ, 724, 448
Narayan, R., Goldreich, P., & Goodman, J. 1987, MNRAS, 228, 1
Okazaki, A. T., & Kato, S. 1985, PASJ, 37, 683
Ou, S., Ji, J., Liu, L., & Peng, X. 2007, ApJ, 667, 1220
Papaloizou, J. C. B., & Pringle, J. E. 1984, MNRAS, 208, 721
Papaloizou, J. C. B., & Pringle, J. E. 1985, MNRAS, 213, 799
Papaloizou, J. C. B., & Pringle, J. E. 1987, MNRAS, 225, 267
Regály, Z., Juhász, A., Sándor, Z., & Dullemond, C. P. 2012, MNRAS, 419, 1701
Takeuchi, T., & Miyama, S. M. 1998, PASJ, 50, 141
Tanaka, H., Takeuchi, T., & Ward, W. R. 2002, ApJ, 565, 1257
Terquem, C. E. J. M. L. J. 2008, ApJ, 689, 532
Umurhan, O. M. 2008, A&A, 489, 953
Umurhan, O. M. 2010, A&A, 521, A25
Umurhan, O. M. 2012, A&A, in press (arXiv:1203.1686)
Varnière, P., & Tagger, M. 2006, A&A, 446, L13
Yang, C.-C., & Menou, K. 2010, MNRAS, 402, 2436
Yu, C., & Li, H. 2009, ApJ, 702, 75
Yu, C., Li, H., Li, S., Lubow, S. H., & Lin, D. N. C. 2010, ApJ, 712, 198
Zhang, H., & Lai, D. 2006, MNRAS, 368, 917